

# The October 2024 Extreme Precipitation Event over Valencia: Storyline Attribution of the Synoptic-Scale Thermodynamic Drivers

Diego A. Campos<sup>1,2</sup>, Katherine Grayson<sup>1</sup>, Ramiro I. Saurral<sup>1,3,4,5</sup>, Sebastian Beyer<sup>6</sup>, Amal John<sup>6</sup>, Matías Olmo<sup>1</sup>, Francisco Doblas-Reyes<sup>1,7</sup>

5 <sup>1</sup>Barcelona Supercomputing Center, Barcelona, Spain

<sup>2</sup>Facultat de Física, Universitat de Barcelona, Barcelona, Spain

<sup>3</sup>CONICET-Universidad de Buenos Aires. Centro de Investigaciones del Mar y la Atmósfera (CIMA), Buenos Aires, Argentina

10 <sup>4</sup>Facultad de Ciencias Exactas y Naturales, Departamento de Ciencias de la Atmósfera y los Océanos, Universidad de Buenos Aires, Buenos Aires, Argentina

<sup>5</sup>CNRS-IRD-CONICET-UBA. Instituto Franco-Argentino para el Estudio del Clima y sus Impactos (IRL 3351 IFAECI), Buenos Aires, Argentina

<sup>6</sup>Alfred-Wegener-Institut, Helmholtz-Zentrum für Polar- und Meeresforschung (AWI), Bremerhaven, Germany

<sup>7</sup>Institució Catalana de Recerca i Estudis Avançats, Barcelona, Spain

15 *Correspondence to:* Diego A. Campos (diego.campos@bsc.es)

**Abstract.** In late October 2024, the western Mediterranean (WMed) region experienced an extreme precipitation event (EPE) centred over Valencia, southeastern Spain, associated with a quasi-stationary cut-off low (COL), producing record rainfall, flash floods, and severe societal impacts. The COL generated an atmospheric-river-like moisture plume from northwestern Africa, while additional moisture originated from the warm Mediterranean Sea. Interaction with regional orography under a highly unstable environment, favoured deep convection and intense local rainfall. To assess the influence of anthropogenic climate change on the synoptic-scale thermodynamic evolution of the event, we analyse high-resolution (~9 km) storyline simulations from the European Union’s Destination Earth initiative, using the coupled IFS-FESOM model spectrally nudged with ERA5. Two climate scenarios are compared: Factual (present-day) and Counterfactual (~1950), isolating thermodynamic responses while keeping large-scale circulation fixed. Long-term IFS-FESOM and ERA5 datasets provide a climatological reference for event extremeness. Results show that the synoptic configuration alone was sufficient to produce extreme rainfall, but human-induced warming substantially enhanced its magnitude. Moisture content and transport increased by 18–24%, convective instability by ~25%, and precipitation over Valencia increased by ~20% in the Factual scenario. Sea surface temperatures in the Western Mediterranean were ~2°C warmer, amplifying evaporation. Peak precipitation rates exhibited nonlinear amplification, on 29 October were about 36% higher in the Factual scenario, exceeding the Clausius–Clapeyron scaling expected from the mean warming between scenarios. These findings indicate that anthropogenic warming can intensify EPEs in the WMed even when synoptic drivers alone would generate extreme rainfall, highlighting thermodynamic amplification as a key mechanism in Mediterranean flood events. High-resolution, physically consistent storyline simulations offer a robust framework for event-based attribution and improve understanding of future climate risks in vulnerable coastal regions.

## 35 1 Introduction

The Western Mediterranean (WMed) has been identified as a prominent climate change hotspot characterised by rapid warming (Campos et al., 2025; Cos et al., 2022; Giorgi, 2006; Lionello & Scarascia, 2020; Tuel & Eltahir, 2020) and increasing risk of extreme precipitation events (EPEs; Lionello & Scarascia, 2020; Olmo et al., 2025; Ribes et al., 2019; Trambly & Somot, 2018; Zittis et al., 2021). In late October 2024, an episode of exceptionally heavy rainfall impacted the southeastern Iberian Peninsula, with the Valencia region experiencing catastrophic flooding where some locations recorded more than 600 mm of precipitation within a few hours (AEMET, 2024). The event resulted in more than 200 fatalities and billions of euros in damages (Llasat, 2024; Martin-Moreno et al., 2025). At the synoptic scale, the event was associated with a quasi-stationary cut-off low (COL, locally referred to as a DANA) interacting with a warm moisture-rich Mediterranean environment (Huang et al., 2025; Saurral et al., 2026), a configuration widely recognised as conducive to extreme precipitation in the region (Nieto Ferreira, 2021; Porcù et al., 2007; Saurral et al., 2025). Given the strong thermodynamic influence of atmospheric moisture on Mediterranean EPEs, the Valencia EPE has become a prominent case study for investigating how anthropogenic climate change may have modified the physical environment supporting extreme precipitation.

Recent attribution studies of the October 2024 Valencia EPE have applied a range of methodological approaches, leading to partly differing, but complementary, conclusions regarding the influence of anthropogenic climate change. Probabilistic attribution approaches, for example, are particularly valuable for quantifying changes in event likelihood and intensity, although their application to highly exceptional precipitation events can be constrained by limited sampling of comparable events and by sensitivity to the event definition. Applying this framework, WWA (2024) estimated that precipitation extremes similar to those observed during the Valencia EPE were approximately 12% more intense and about twice as likely under present-day warming conditions relative to a 1.3°C cooler counterfactual climate. By contrast, Barriopedro et al. (2025), using a broadly comparable probabilistic method and counterfactual definition, reported only weak and statistically non-significant changes in probability and intensity. Other studies adopted circulation-conditioned attribution frameworks to separate thermodynamic and dynamic contributions to the event, which is particularly useful for contextualising an EPE under similar circulation patterns in a counterfactual (usually mid-20th century) climate. Using circulation analogues, Faranda et al. (2024) and Barriopedro et al. (2025) (who applied several attribution methods for the same event), reported modest increases in precipitation and atmospheric moisture under present-day conditions, although with substantial uncertainty and limited statistical significance. Similarly, Oldham-Dorrington & Messori (2026), found no robust changes in either the frequency of the atmospheric pattern associated with the event or its relationship with extreme precipitation.

Other studies have applied event-based storyline approaches (Shepherd et al., 2018) to investigate how anthropogenic climate change modified the thermodynamic characteristics of the Valencia EPE. In contrast to probabilistic and circulation-

analogue approaches, these methods focus less on changes in the event likelihood and more on how present-day warming altered the physical environment associated with the event. Using a pseudo-global-warming storyline approach and high-resolution regional modelling, [Calvo-Sancho et al. \(2026\)](#) focused on the convective storm affecting Valencia on 29 October, examining how climate change modified local thermodynamic and convective processes. Their results showed increases of approximately 12% in precipitable water and 22% in convective instability under present-day climate conditions relative to a pre-industrial climate, leading to rainfall intensification rates exceeding Clausius-Clapeyron (CC) scaling. Similarly, [Barriopedro et al. \(2025\)](#), using AI-based weather forecasts combined with a pseudo-global-warming storyline method, investigated how anthropogenic warming modified the regional-scale thermodynamic drivers during the peak of the Valencia EPE. Their results indicated precipitation increases of up to 20%, together with enhanced low-level moisture transport under present-day climate conditions. Taken together, these studies consistently point toward substantial thermodynamic amplification of the event under present-day warming conditions.

While previous studies using the storyline approach have primarily examined the local and regional thermodynamic amplification of precipitation during the peak of the Valencia EPE, important uncertainties remain regarding how anthropogenic warming modified the associated broader synoptic-scale thermodynamic environment. In particular, the role of climate change in shaping the evolution of large-scale moisture transport, atmospheric instability, and Mediterranean thermodynamic preconditioning prior to the most intense rainfall remains insufficiently explored. This aspect is particularly relevant for EPEs associated with COLs, whose precipitation intensity is strongly conditioned by the interaction between upper-level cold-air and the transport of warm, moist air beneath the upper-level low ([Barrett et al., 2016](#); [Bozkurt et al., 2016](#); [Insua-Costa et al., 2019](#); [Muñoz & Schultz, 2021](#); [Tsuji & Takayabu, 2019](#); [Valenzuela et al., 2022](#)). Moreover, in the WMed, these processes can be further amplified by anomalously warm sea surface temperatures ([Saurral et al., 2026](#)). Understanding how climate change modifies these large-scale thermodynamic and moisture transport processes therefore requires attribution frameworks capable of preserving the observed dynamical configuration of the event while isolating the thermodynamic influence of anthropogenic warming.

Spectral nudging has emerged as a particularly useful technique for reproducing dynamically consistent storylines in both regional and global climate models ([Feser & Shepherd, 2025](#); [Van Garderen et al., 2021](#)). By constraining the large-scale atmospheric circulation toward reanalysis data while allowing thermodynamic processes and mesoscale variability to freely evolve, spectral nudging provides a suitable framework for investigating how anthropogenic warming modifies the evolution of specific EPEs. Within the European Union's Destination Earth initiative (DestinE ClimateDT; [Doblas-Reyes et al., 2026](#); [Hoffmann et al., 2023](#); [Wedi et al., 2022](#)), kilometre-scale coupled global storyline simulations using the IFS-FESOM model ([Rackow et al., 2025](#)) are available as continuous factual and counterfactual scenarios from 2017 onward using spectral nudging toward ERA5 data ([John et al., 2026](#)). Unlike the storyline using the pseudo-global-warming approach, the DestinE ClimateDT global storyline simulations enable the study of the large-scale thermodynamic evolution associated with EPEs

within a dynamically consistent framework beyond region-specific or event-specific experimental setups. Moreover, the coupled atmosphere-ocean configuration allows interactive air-sea feedbacks and evolving ocean conditions, rather than relying on prescribed sea surface temperatures. In addition, the kilometre-scale resolution allows both the synoptic-scale drivers and the regional-to-local precipitation evolution to be examined within a unified modelling framework. Despite this potential, such global kilometre-scale storyline simulations have not yet been systematically explored in extreme event attribution studies (e.g., [Grayson et al., 2026](#)).

In this paper, we investigate the influence of anthropogenic climate change on the synoptic-scale thermodynamic environment associated with the October 2024 Valencia EPE, with a particular focus on the spatiotemporal evolution of atmospheric moisture, moisture transport, and instability before and during the event. To this end, we analyse spectrally nudged kilometre-scale global storyline simulations from DestinE ClimateDT under Factual (present-day) and Counterfactual (~1950s) climate conditions using the coupled IFS-FESOM model nudged with ERA5 reanalysis data. Our study complements previous statistically-derived and regional-to-local storyline attribution analyses by being the first focusing on the evolution of the synoptic-scale thermodynamic conditions associated with the event before and during the rainfall peak with global km-scale model simulations. More broadly, this work contributes to the growing recognition that robust extreme event attribution benefits from the combination of multiple methodological approaches addressing complementary aspects of the climate system and the event under investigation ([Thompson et al., 2025](#); [Van Garderen & León-FonFay, 2026](#)). [Section 2](#) describes the data and methods used in the study. [Section 3](#) presents the analysis results. Finally, in [Section 4](#), the main results are discussed, and questions for future studies are raised.

## 2 Data and Methods

### 2.1 Model data

In this work, we analyse the spectrally-nudged storyline simulations conducted with the coupled global climate model IFS-FESOM from the DestinE ClimateDT initiative. This modelling framework couples the Integrated Forecasting System (IFS, cycle 48r1; [ECMWF, 2023](#)), developed by ECMWF, for the atmosphere, land, and waves, with the Finite volumE Sea Ice-Ocean Model (FESOM2, version 2.5) from the Alfred Wegener Institute. The setup used corresponds to the ClimateDT configuration ([Rackow et al., 2025](#)). The atmospheric component has a horizontal resolution of roughly 9 km (TCO1279 spectral resolution) with 137 vertical levels. The ocean component has 70 vertical levels and uses a horizontal resolution (unstructured NG5 mesh) that smoothly transitions from about 12 km in the tropics to 4.5 km in dynamically active regions and polar areas ([Danilov et al., 2017](#); [Scholz et al., 2019](#)).

The spectral nudging scheme used to constrain the large-scale circulation towards the observations in the simulations was made following the methodology of [Sánchez-Benítez et al. \(2022\)](#). This approach relaxes large-scale vorticity and

divergence in the model towards ERA5 reanalysis data between 700 and 100 hPa up to wavenumber T60. Additionally, a 1-  
135 hour e-folding was employed to maintain consistency with the observed large-scale flow, while allowing the model to  
simulate small-scale processes freely (John et al., 2026). In this way, the large-scale flow above 700 hPa remains consistent  
with ERA5, allowing changes in the nudged simulations to be mainly attributed to thermodynamic features and small-scale  
dynamics.

140 Two climate scenarios are considered in this study: Factual (present-day climate) and Counterfactual (cooler ~1950s  
climate). The scenarios differ in their ocean initial states and boundary conditions (i.e., external climate forcing and  
background climate state), allowing the evaluation of how identical meteorological events would evolve under different  
climate states:

- Counterfactual (cooler ~1950s) – representing an early-industrial-like state based on 1950 boundary conditions with  
145 CMIP6-historical radiative forcing. In this experiment, the forcing is held fixed at its 1950 values for the entire  
2017-2024 simulation period.
- Factual (present-day) – representing current conditions (2017–2024) forced with the SSP3-7.0 scenario. In this case,  
the external forcing is transient and evolves year by year.

These scenarios were driven by the same spectrally-nudged large-scale circulation and initial atmospheric conditions (01-01-  
150 2017 ERA5) and were run until 31-12-2024.

For each simulation, a five-year ocean spin-up was performed using stand-alone FESOM2 integrations (1945–1949 for the  
Counterfactual and 2012–2016 for the Factual). For details, please refer to John et al. (2026).

To ensure robustness in the differences between the Factual and Counterfactual experiments, we use four additional  
155 ensemble members for each variable, branched from the main simulation. Following the lag-based ensemble approach of  
Brenowitz et al. (2025), spectral nudging is temporarily disabled at the beginning of the simulation period for different  
durations in each member before being reactivated using the July 2024 restart files. Specifically, nudging is switched off  
from 1 July 2024 for 1 day in member #1, 2 days in member #2, 3 days in member #3, and 4 days in member #4, after which  
nudging is re-enabled for the remainder of the simulation period. This procedure allows the model to evolve freely for a  
160 short period, creating slightly different atmospheric states that stabilise during the subsequent nudged period and provide a  
representation of internal variability. The limited ensemble size is primarily due to the high computational cost of conducting  
global km-scale simulations.

## 2.2 Synoptic variables

For our analyses, we use hourly model output from 00 UTC on 24 October 2024 to 23Z on 31 October 2024, covering the domain 35°W–20°E and 10–60°N. The variables considered include the zonal and meridional wind components ( $u$ ,  $v$ ), vertical velocity ( $\omega$ ), specific humidity ( $q$ ), and geopotential height, at the following pressure levels: 1000, 925, 850, 700, 600, 500, 400, 300, 250, 150, 100, and 70 hPa. Additionally, we analysed precipitation rate, mean sea level pressure (MSLP), 2-meter air temperature, total column water vapour (TCWV), sea surface temperature (SST), and evaporation. From these variables, we further derived the Most Unstable Convective Available Potential Energy (hereafter called CAPE) using the MetPy Python library (May et al., 2022) and Integrated Water Vapour Transport (IVT) using Eq. (1),

$$IVT = \frac{1}{g} \int_{1000 \text{ hPa}}^{300 \text{ hPa}} \mathbf{V}qdp, \quad (1)$$

where  $g$  is the acceleration of gravity,  $\mathbf{V} = (u, v)$  is the wind components, and  $dp$  is the depth of atmospheric layers in terms of pressure.

To disentangle the dynamic and thermodynamic contributions to surface evaporation, we diagnosed wind stress and saturation deficit as independent controlling factors (Zhang, 1997). The dynamic component was represented by the surface wind stress, computed as

$$\tau = \rho C_D V^2 \quad (2)$$

where  $\rho$  is air density,  $C_D$  is the drag coefficient, and  $V^2$  is the 10-m wind speed. The thermodynamic contribution was quantified through the saturation deficit, defined as the difference between the saturation specific humidity at sea surface temperature and the near-surface specific humidity ( $\Delta q = q_s - q_a$ ). By analysing these two terms separately, we isolate the relative roles of dynamical forcing and thermodynamic gradients in shaping evaporation evolution.

To provide observational and reanalysis context, we also obtained the same set of atmospheric variables from ERA5 via the Copernicus Climate Data Store (Copernicus Climate Change Service, 2018). Daily SSTs were taken from the NOAA OISSTv2 database (Huang et al., 2021). Daily precipitation was derived from the Multi-Source Weighted-Ensemble Precipitation (MSWEP, Beck et al., 2019) and E-OBS (Cornes et al., 2018) datasets, as well as from ground-based observations provided by the Spanish Meteorological Agency (Agencia Estatal de Meteorología, AEMET) and the Valencian Meteorological Association (Associació Valenciana de Meteorologia, AVAMET). The full list of stations is provided in Supplementary Table 1.

To analyse the pathways of air parcels reaching Valencia on the day of the event, and to support the definition of regions of interest for the subsequent attribution analysis, we used the online version of the HYSPLIT model (Stein et al., 2015), available through the NOAA Air Resources Laboratory website. An analysis of 72-hour backward trajectories was

195 performed for air parcels arriving at Valencia (39.47°N, 0.37°E) at 12Z on 29 October, at four different arrival heights: 250, 1000, 2000, and 3000 m above sea level (ASL). The trajectories were computed using data from the NCEP Global Data Assimilation System (GDAS). For each arrival height, an ensemble of 27 members was generated to account for trajectory uncertainty. The resulting trajectory patterns were used to identify the main transport pathways feeding the event, which guided the selection of the regions used in the attribution framework.

### 200 **2.3 Long-term simulation**

To assess the magnitude and uniqueness of the event, we placed it into a long-term climatological context. For this purpose, we used an extended IFS-FESOM reference climate simulation (hereafter referred to as IFS-FESOM) covering the period 1950-2014, obtained from the European Eddy RIch Earth System Models (EERIE) project (Ghosh et al., 2025). Unlike the spectrally-nudged simulations described above, this experiment was performed without spectral nudging, allowing the model  
205 to freely evolve. Apart from this difference, all other aspects of the experimental setup remained identical, including the atmospheric and oceanic components, parameterisations, and horizontal and vertical resolutions (Rackow et al., 2025). This consistency allows the IFS-FESOM simulation to be used as a physically coherent climatology to contextualise the storyline scenarios. To reduce storage and computational costs, the output data were regridded onto a regular 0.25°x0.25° grid.

210 For the present analysis, daily values of selected key variables during the Valencia EPE were compared with their corresponding October-November daily values from the 1950-2014 IFS-FESOM simulation, as well as from ERA5 over the same reference period. Percentile-based thresholds (e.g., 5th or 95th percentiles) were calculated from the October–November daily values over the reference period, separately for IFS-FESOM and ERA5. This percentile-based comparison with a long reference simulation follows the climatological framing used in Van Garderen et al. (2021) to contextualise event  
215 extremeness. In our case, we use a bi-monthly climatology because including September (i.e., using the SON season) would incorporate markedly warmer and drier conditions that might not be representative of the late-October environment in which the event developed (e.g., Figure 3 in Campos et al., 2025). For precipitation, the maximum daily precipitation index (Rx1day) was computed as the highest daily precipitation amount within each month, following the Expert Team on Climate Change Detection and Indices (ETCCDI; Zhang et al., 2011) definition, over Valencia. This Rx1day was then compared  
220 with the 95th percentile from the same reference period.

## 2.4 Event attribution

To assess the influence of climate change on the variables that influenced the Valencia EPE, we compared the Factual and Counterfactual scenarios by subtracting the latter from the former. We then calculated the relative changes following Eq. (3), which quantifies the percentage difference between the Factual (present-climate) and Counterfactual (colder-climate) values, normalised by the Counterfactual state.

$$\text{Relative change} = \frac{\text{Factual} - \text{Counterfactual}}{\text{Counterfactual}} \times 100 \quad (3)$$

To assess whether the differences between scenarios lie outside the range of internal variability, we applied a signal-to-noise approach following the methodology of Van Garderen et al. (2021). The method uses all possible pairwise combinations of ensemble members to compute differences both within and between scenarios. The inter-scenario differences (Factual – Counterfactual) represent the signal, while the intra-scenario differences (Factual – Factual and Counterfactual – Counterfactual) represent the noise. Following Van Garderen et al. (2021), a significant signal-to-noise ratio is identified when the median of the signal distribution lies outside the inter-quartile range of the noise.

## 3 Results

### 3.1 Event description and model validation

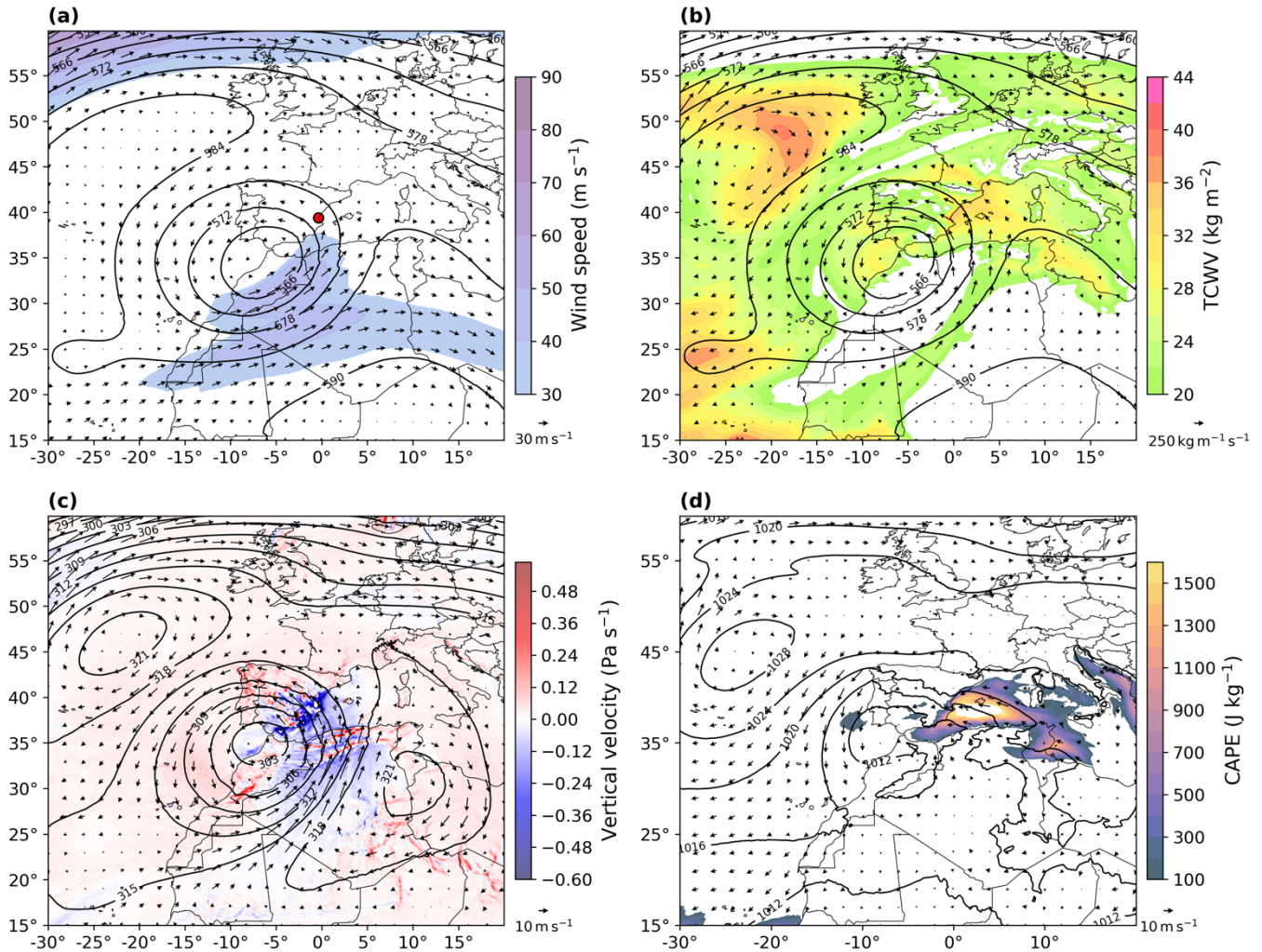
The devastating EPE in Valencia (represented by the red dot in Fig. 1a) occurred on 29 October 2024. In this section, the event is described based on the Factual simulation from the DestinE ClimateDT model, which provides the main reference for the analysis. ERA5 is included for intercomparison purposes and is shown in the Supplementary Material.

On this day, in the Factual scenario (Fig. 1), an upper-level COL is located over the southwestern Iberian Peninsula, centred near 35°N, 5°W. This configuration persisted for several days (not shown), with the COL drifting slightly southwestward from the central Iberian Peninsula between 27 and 29 October, thereby maintaining its quasi-stationary character. This persistent evolution is consistent with that found in ERA5, as expected given the spectral nudging applied in the simulation (Fig. S1 in the Supplement).

Over the Mediterranean coast of Spain, TCWV (shaded colours in Fig. 1b) exceeds 30 kg m<sup>-2</sup>, enhanced by a plume of moisture transported from the subtropical Atlantic across northwestern Africa in an atmospheric-river-like (AR-like) structure. This plume, located along the eastern flank of the COL, exhibits local IVT magnitudes exceeding 500 kg m<sup>-1</sup> s<sup>-1</sup> (Fig. 1b). The moisture flux reaches the Valencian coast almost perpendicularly, favouring moisture convergence and orographic lifting as the low-level flow interacts with the local topography (Fig. 1c; see Fig. S2 in the Supplement for the

250 model's topography). This moist environment off the Valencian coast is also unstable, with CAPE values exceeding  $1500 \text{ J kg}^{-1}$  (Fig. 1d).

The synoptic configuration in the Factual scenario shows good agreement with ERA5, not only for the nudged dynamical fields, such as geopotential height, but also for thermodynamic variables like TCWV (Fig. S3 in the Supplement). The main discrepancy arises from an underestimation of CAPE over land in the Factual scenario compared to ERA5. This difference might be related to the coarser vertical resolution used to compute CAPE in the simulation (11 levels in the Factual scenario versus 27 levels in ERA5).



260 **Figure 1:** Daily composite for the 29 October 2024 from the Factual scenario for (a) 500-hPa geopotential height (contours, dam), 300-hPa wind (arrows,  $\text{m s}^{-1}$ ) and 300-hPa wind speed (colours,  $\text{m s}^{-1}$ ), (b) 500-hPa geopotential height (contours, dam), integrated water vapour transport (IVT, arrows,  $\text{kg m}^{-1} \text{ s}^{-1}$ ) and total column water vapour (TCWV, colours,  $\text{kg m}^{-2}$ ), (c) 700-hPa

265 geopotential height (contours, dam), 700-hPa wind (arrows,  $\text{m s}^{-1}$ ) and vertically-averaged vertical velocity (colours,  $\text{Pa s}^{-1}$ ), and (d) mean sea level pressure (MSLP, contours, hPa), 1000-hPa wind (arrows,  $\text{m s}^{-1}$ ) and most unstable convective available potential energy (CAPE, colours,  $\text{J kg}^{-1}$ ). The red dot on (a) shows the approximate location of Valencia.

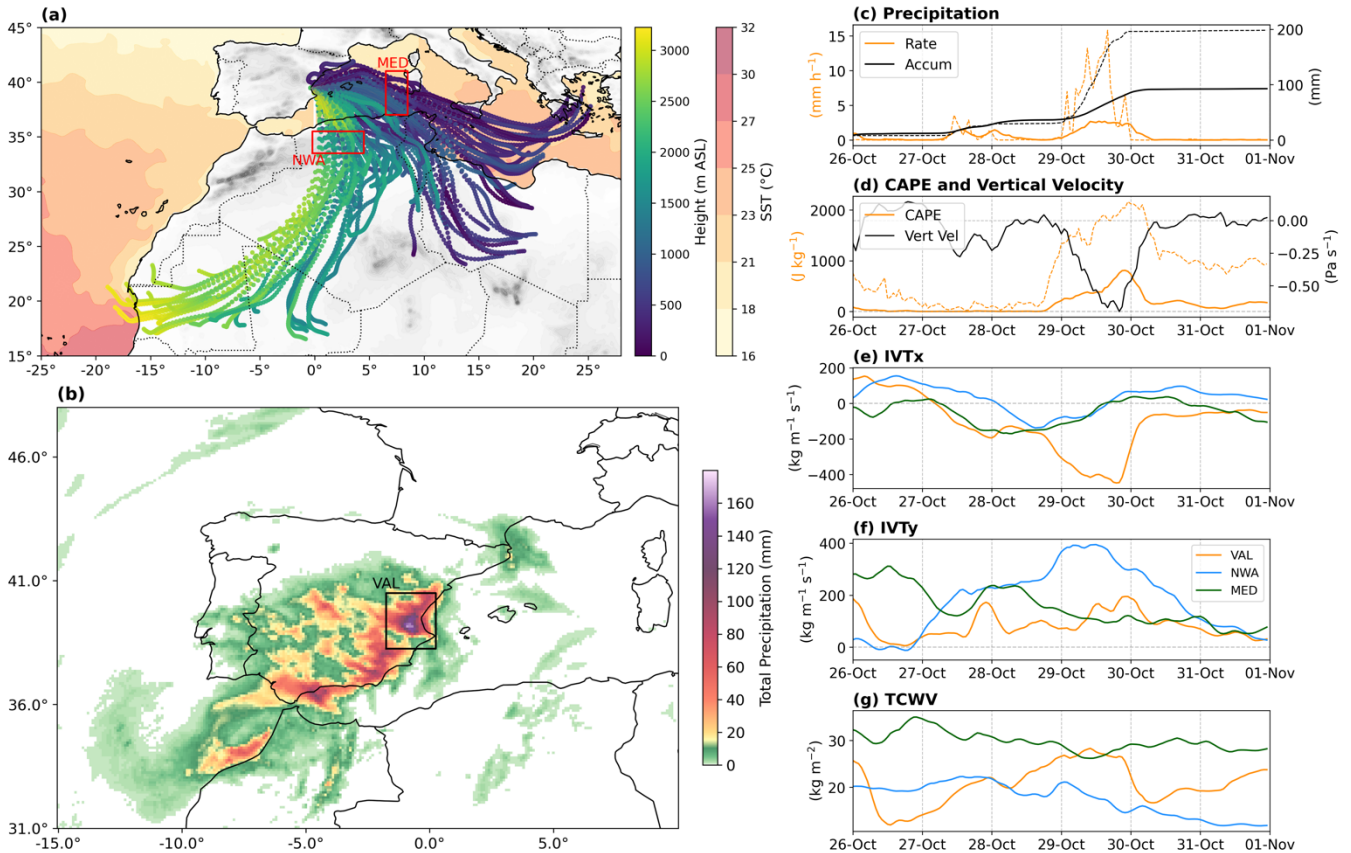
Two main air parcel pathways can be identified reaching the Valencia area on the 29th. The first pathway, associated with the AR-like structure, originates over the subtropical Atlantic, crosses northwestern Africa at mid-tropospheric levels (approximately 2000–3000 m ASL), and arrives over Valencia at a similar altitude. In contrast, the second pathway travels at 270 low levels (around 500 m ASL) across the Mediterranean Sea, reaching Valencia near the surface (Fig. 2a). The relatively warm SSTs over the Mediterranean (around  $24\text{ }^{\circ}\text{C}$  during the week of the event, Fig. 2a) favour the high values of TCWV and CAPE observed in the region (Fig. 1b-d). To further investigate the role of these two moisture pathways on the precipitation in Valencia, and how they differ across climate scenarios, we define two regions: the Northwestern Africa region (NWA;  $33.45^{\circ}$ – $35.45^{\circ}\text{N}$ ;  $0.20^{\circ}\text{W}$ – $4.50^{\circ}\text{E}$ ) and the Mediterranean region (MED;  $37.05^{\circ}$ – $41.05^{\circ}\text{N}$ ;  $6.50^{\circ}$ – $8.50^{\circ}\text{E}$ ), as 275 shown in red boxes in Fig. 2a.

The spatial precipitation pattern on 29 October in the Factual scenario is shown in Fig. 2b. A broad area over southern Iberia experiences rainfall during the day, with the highest amounts concentrated over the Valencia region, where a local maximum of approximately 180 mm is simulated. This pattern closely resembles that from ERA5, although the higher horizontal 280 resolution of the Factual simulation provides greater spatial detail, particularly in capturing the influence of topography on precipitation. In contrast, E-OBS and MSWEP display a more homogeneous spatial distribution (Fig. S4 in the Supplement). Despite the realistic spatial distribution, the Factual simulation underestimates total precipitation compared to local ground stations in the Valencia region, which recorded more than 600 mm in 24 hours (Table S1 and Fig. S5 in the Supplement). Therefore, in this study, we focus on the synoptic environment and the regional characteristics of precipitation over 285 Valencia, and define the Valencia box, VAL ( $38.25^{\circ}$ – $40.50^{\circ}\text{N}$ ;  $1.75^{\circ}\text{W}$ – $0.25^{\circ}\text{E}$ , black box in Fig. 2c) for further analysis.

Between 24 and 31 October, the Valencia region (VAL) accumulated an average of approximately 100 mm of precipitation, with local maxima reaching around 200 mm. Most of this rainfall occurred on 29 October, when the highest precipitation rates were simulated, with mean values of about  $2\text{ mm h}^{-1}$ , and local peaks exceeding  $10\text{ mm h}^{-1}$  (Fig. 2c). The precipitation 290 maximum on 29 October coincides with a period of enhanced atmospheric instability over VAL (Fig. S7 in the Supplement), characterised by mean CAPE values near  $600\text{ J kg}^{-1}$ , local maxima close to  $2000\text{ J kg}^{-1}$ , and a (negative) peak in vertical velocity (Fig. 2d).

These precipitation and instability peaks are closely linked to the evolution of the IVT and TCWV over the region. The 295 westward (negative) zonal component of the IVT over VAL gradually increases with time, reaching a maximum of about  $400\text{ kg m}^{-1}\text{ s}^{-1}$  on 29 October (Fig. 2e). At the same time, the northward (positive) meridional component (IVTy) over the

northwestern Africa region (NWA) also peaks near  $400 \text{ kg m}^{-1} \text{ s}^{-1}$ , associated with the AR-like moisture plume (Fig. 2f). The biggest contribution from the Mediterranean region (MED) appears to occur one to two days earlier, when the IVT reaches its maximum with a southeasterly orientation (Fig. 2e-f). The maximum TCWV over VAL is observed on 29 October, with values close to  $30 \text{ kg m}^{-2}$ , followed by a rapid decrease associated with the dissipation of the NWA moisture inflow and the peak in precipitation on the same day (Fig. 2g). In contrast, TCWV over the MED remains relatively steady through time, suggesting it is mainly governed by local processes rather than remote moisture transport (Fig. 2g).



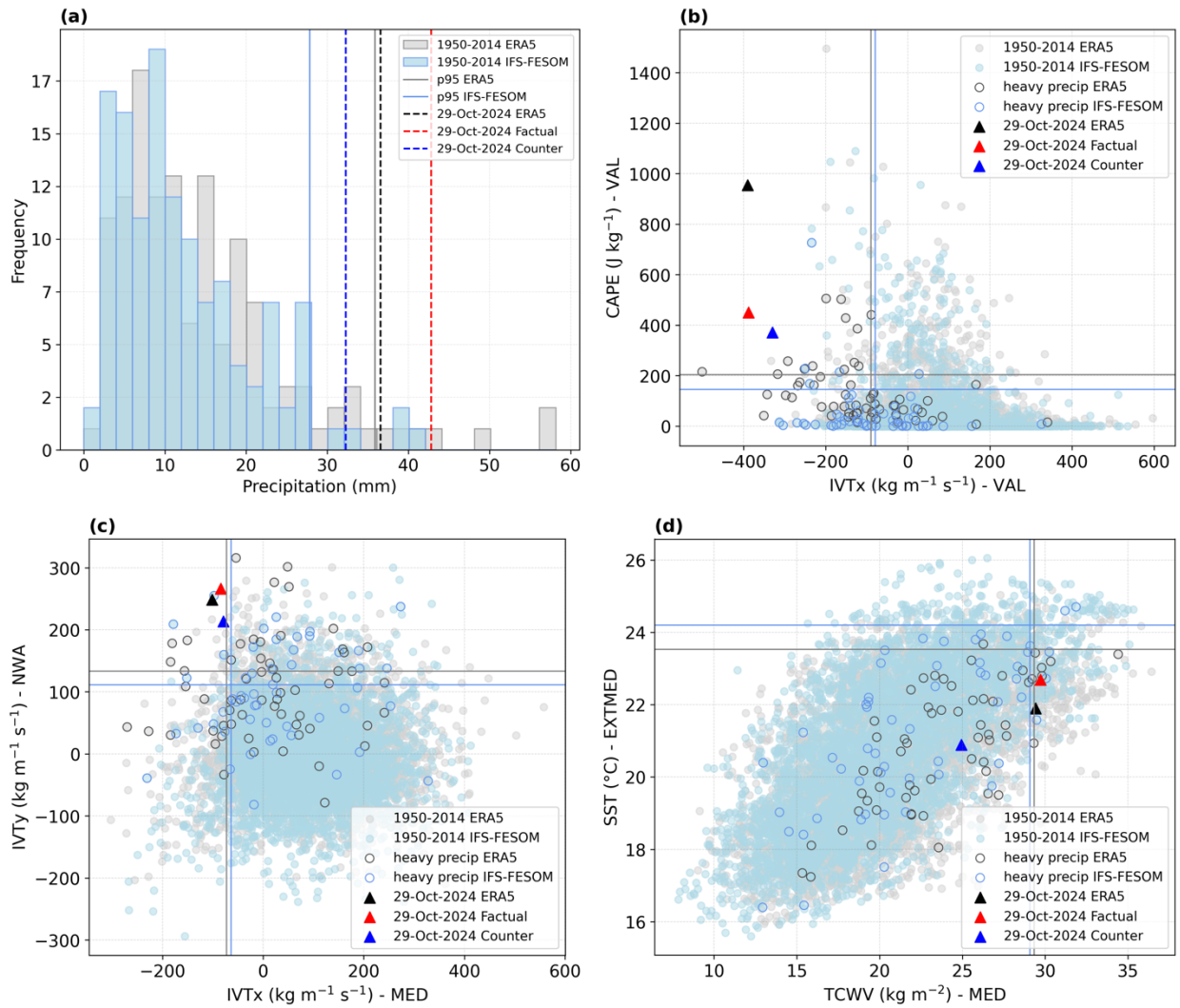
305 **Figure 2:** (a) 72-hour backward trajectories from the HYSPLIT model for air parcels arriving in Valencia at 12Z on 29 October, and 7-day mean (24-30 Oct) SSTs ( $^{\circ}\text{C}$ ) from NOAA OISSTv2. Red boxes indicate the Mediterranean (MED) and Northwestern Africa (NWA) boxes. (b) 24-hour accumulated precipitation on 29 October from the Factual scenario, with the Valencia (VAL) box shown in black. (c) Hourly precipitation rate (orange) and accumulated precipitation (black) over the Valencia box. Solid lines indicate the box mean, and dashed lines indicate the grid cell with the highest accumulation. Accumulated precipitation is computed starting at 00 UTC on 24 October. (d) Vertically-averaged vertical velocity (black) and CAPE (orange) over the Valencia box. Solid lines show the box mean, and the orange dashed line indicates the highest hourly CAPE within the box. (e) Hourly mean zonal IVT (IVTx) over VAL (orange), NWA (blue), and MED (green). (f) As in (e), but for meridional IVT (IVTy). (g) As in (f), but for TCWV.

310

### 315 3.2 Long-term perspective

We now analyse the key variables associated with the Valencia EPE, described in [Section 3.1](#), within a climatological context. For this purpose, we used the long IFS-FESOM simulation and ERA5 reanalysis over the 1950-2014 period as reference datasets; ERA5 provides an observational reference, while the long IFS-FESOM run offers a model-consistent climatology for the storyline framework. The extremeness of the event was assessed using the maximum daily precipitation index (Rx1day) over the VAL region ([Fig. 3a](#)). During the Valencia EPE, the spatially averaged daily precipitation in the Factual scenario reached nearly 44 mm (red dashed line in [Fig. 3a](#)), exceeding the 95th percentile of the Rx1day distribution in the long IFS-FESOM simulation (~28 mm; thin light blue line in [Fig. 3a](#)). In statistical terms, this indicates that the Valencia EPE qualifies as an extreme event. A similar conclusion is obtained from ERA5, although in this case, the event magnitude exceeds the 95th percentile of ERA5 by a smaller margin than in the IFS-FESOM world (black dashed and grey lines in [Fig. 3a](#)).

320  
325



330 **Figure 3:** (a) Distribution of maximum daily precipitation ( $Rx1day$ ) in Valencia (VAL box) for October–November during 1950–2014 in ERA5 (light grey bars) and IFS-FESOM free run (light blue bars). (b) Daily mean IVTx and CAPE values spatially averaged over VAL for October–November during 1950–2014 in ERA5 (light grey circles) and IFS-FESOM (light blue circles). (c) As in (b), but for the 3-day mean IVTx values spatially averaged over the Mediterranean box (MED) and IVTy over northwestern Africa box (NWA). (d) As in (c), but for TCWV over MED and SST over an extended Mediterranean box (EXTMED;  $36.5^{\circ}$ – $40.5^{\circ}$ N;  $0.0^{\circ}$ – $8.5^{\circ}$ E). Thin vertical lines (light grey for ERA5, light blue for IFS-FESOM) indicate the 5th or 95th percentiles of the 1950–2014 reference period, as appropriate. Dashed vertical lines in (a) and triangles in (b)–(d) denote the values on 29 October for ERA5 (black) and for the Factual (red) and Counterfactual (blue) scenarios. Bordered circles in (b) indicate days with heavy precipitation in VAL (defined as exceeding the 75th percentile). In (c) and (d), bordered circles indicate heavy-precipitation days based on the last day of the 3-day period.

335

If we now apply this analysis as an approximation for a statistical attribution assessment, following a strategy similar to Van Garderen et al. (2021), we can compare the Factual and Counterfactual scenarios within a climatological context. For  $Rx1day$  in VAL, both scenarios exceeded the 95th percentile, although the Counterfactual scenario exhibits a lower magnitude

340

(see red and blue dashed lines in Fig. 3a). This suggests that the event would also have been extreme under a colder climate, although less intense.

345 Following the same approach, but now focusing on a combination of variables associated with the extreme precipitation over VAL, we analysed the daily IVTx and CAPE spatially averaged over this region (Fig. 3b). On the day of the event, a situation characterised by high CAPE and strongly negative IVTx values is observed (black and red triangles in Fig. 3b). Heavy precipitation events in VAL tend to occur under negative IVTx conditions, i.e., an easterly moisture flux from the Mediterranean Sea toward the region, which effectively transports humid air and contributes to convective development; however, CAPE does not appear to be a determining factor in these heavy precipitation events (bordered circles in Fig. 3b). On October 29, both variables exceeded their respective thresholds for statistical extremeness in both the ERA5 and IFS-FESOM datasets. Furthermore, both the Factual and Counterfactual scenarios exceed the 95th percentile, suggesting that the intense zonal moisture flux and atmospheric instability observed on 29 October would have been considered extreme even in the absence of anthropogenic climate change (Fig. 3b).

355

In a similar way, we examine the extremeness of the moisture transport contributions from both NWA and MED. As these regions are distant from VAL and the maximum IVT does not necessarily coincide with the day of heavy precipitation there (see Fig. 2c-g), we use 3-day mean values for each variable. Figure 3c shows the 3-day mean IVTx over MED and IVTy over NWA. During the event, a strong positive IVTy over NWA, typically associated with heavy precipitation in VAL (see bordered circles in Fig. 3c), acts in combination with a strong negative IVTx over MED (Fig. 3c). Both variables reach extreme values, with those in the Factual scenario exceeding the thresholds derived from the long IFS-FESOM simulation, particularly for IVTy in NWA. The same result is obtained when using ERA5 data (Fig. 3c). For both variables, the Counterfactual closely follows the Factual, with values remaining above the extreme threshold. This indicates that the moisture transport from the NWA and MED regions would also have been extreme in a colder climate (Fig. 3c).

365

The final set of variables examined from a long-term perspective are TCWV and SST over the Mediterranean Sea, given their relatively high values during the event (Fig. 2). For TCWV, we use the same MED region defined previously, while for SST, we extend the MED box towards the Valencian coast, defining a new region: the extended Mediterranean box (EXTMED; 36.5°–40.5° N, 0.0° W–8.5° E, see Fig. 5a). This extension is made because, unlike in the analysis of moisture transport (where independence from the NWA box was needed), for SST and evaporation it is more relevant to encompass the marine area directly influencing the Valencia EPE. For both variables, 3-day mean values are used to place their magnitudes in the context of the 1950-2014 reference period, using both IFS-FESOM and ERA5 datasets (Fig. 3d). Most heavy precipitation days in VAL do not exceed the 95th percentiles of TCWV and SST over the MED region, suggesting that these are not necessary conditions for extreme precipitation in VAL (see bordered circles in Fig. 3d). During the Valencia EPE of October 2024, TCWV over MED slightly exceeded the 95th percentile of the reference period in both the

375

IFS-FESOM Factual scenario and ERA5, whereas SST over the EXTMED region did not (Fig. 3d). Interestingly, TCWV over MED is not extreme in the Counterfactual scenario, indicating that anthropogenic climate change substantially contributed to the unusually high moisture content over MED during the 29 October event (Fig. 3d).

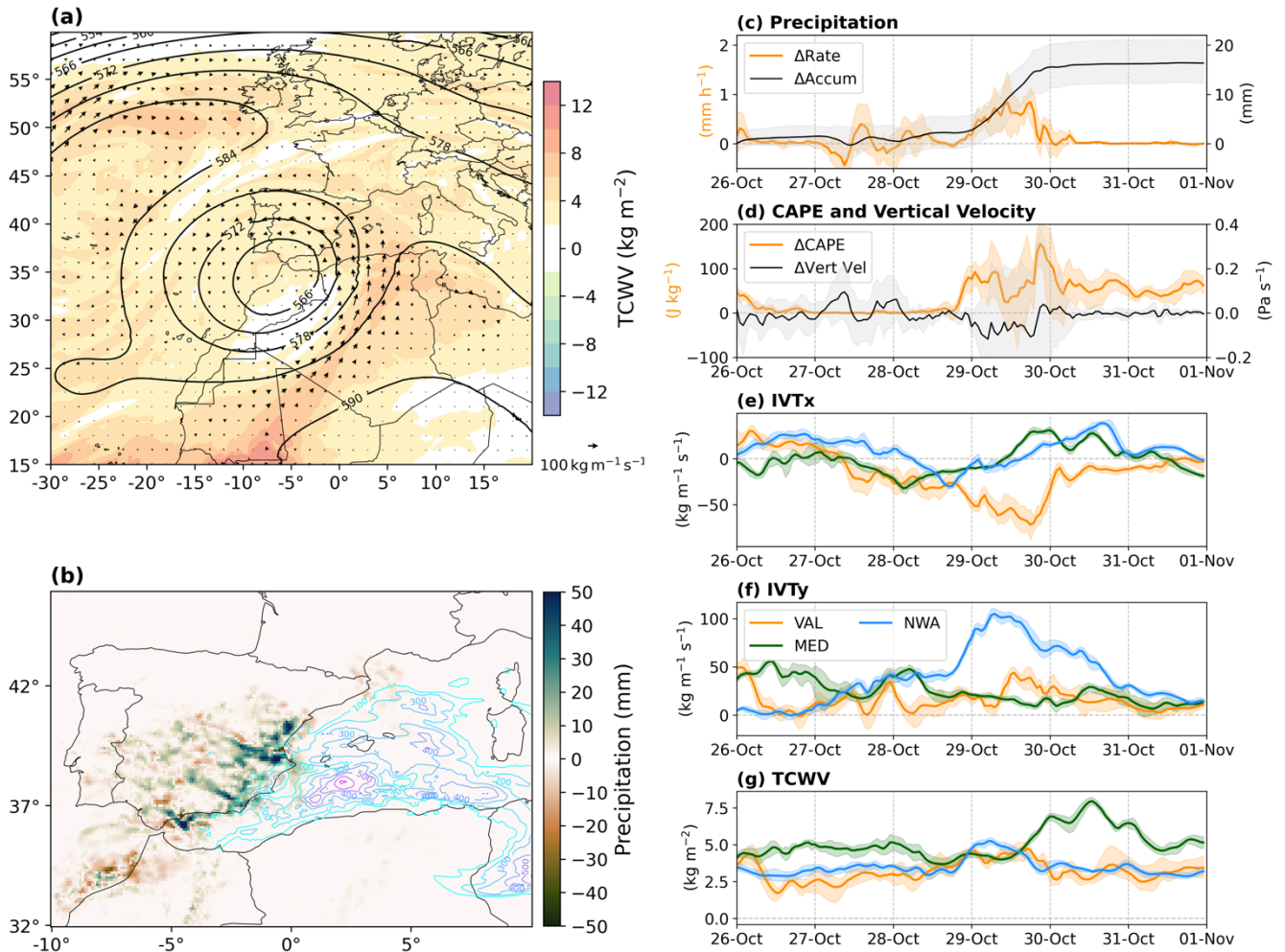
### 380 3.3 Factual–Counterfactual comparison

In this section, we analyse the role of climate change in shaping the synoptic environment and precipitation over Valencia during the event by comparing the Factual and Counterfactual scenarios. On 29 October, positive TCWV anomalies are found across the entire domain, particularly within the AR-like moisture plume along the eastern flank of the COL circulation (Fig. 4). In this region, TCWV exceeds the Counterfactual values by more than  $8 \text{ kg m}^{-2}$ , and IVT increases by  
385 over  $100 \text{ kg m}^{-1} \text{ s}^{-1}$  in the Factual scenario (Fig. 4a). We use here the geopotential height from the Factual scenario to depict the COL circulation, as no displacement in the COL position is found between scenarios due to the spectral nudging applied in the simulations. Nevertheless, we observe an increase in the COL 1000-500 hPa thickness from the Counterfactual to the Factual scenario, consistent with the thermodynamic response to anthropogenic global warming (Fig. S6 and Fig. S7b in the Supplement; IPCC (2023); Santer et al. (2017)).

390

The enhancement of the AR-like moisture plume reaches its maximum on 29 October, with a southerly IVTy component over NWA increasing by about  $100 \text{ kg m}^{-1} \text{ s}^{-1}$  (Fig. 4f). This intensified moisture transport subsequently impacts VAL, where IVTx increases by nearly  $70 \text{ kg m}^{-1} \text{ s}^{-1}$  (Fig. 4e), consistent with an increase in lower-level moisture availability (Fig. S7b in the Supplement). The IVT originating from the Mediterranean also strengthens in the Factual scenario, although to a  
395 lesser extent (Fig. 4e-f). In addition, the TCWV shows higher values across all regions due to climate change (Fig. 4g), indicating a general increase in moisture availability and transport.

This enhanced moisture supply has a direct effect on precipitation. On 29 October, precipitation increases markedly along the southeastern coast of Spain, with local maxima exceeding 40-50 mm over the VAL area (Fig. 4b). The higher  
400 precipitation rate throughout the day results in an additional 15-20 mm of rainfall accumulation over VAL during the event (from 24 to 31 October, Fig. 4c). In parallel, atmospheric instability intensifies over the Mediterranean Sea, with local CAPE differences reaching  $\sim 500 \text{ J kg}^{-1}$  (Fig. 4b). Although the CAPE increase is less pronounced over land, values exceeding  $100 \text{ J kg}^{-1}$  are observed over VAL on 29 October (Fig. 4d). The vertically-averaged vertical velocity exhibits a tendency toward enhanced upward motion over VAL across scenarios on 29 October; however, this signal shows substantial inter-ensemble  
405 spread (Fig. 4d), preventing a robust separation across scenarios. This behaviour is consistent with changes being primarily confined to the mid- to upper-tropospheric levels (approximately 600–300 hPa), while the low-level flow and its interaction with the regional topography remain broadly similar across scenarios (Fig. 5a).



410 **Figure 4:** (a) Composite of mean daily differences (Factual – Counterfactual) on 29 October for IVT (arrows) and TCWV  
 (shading). Contours show the daily mean 500-hPa geopotential height (dam) in the Factual scenario (as in Figure 1a–b). (b) Mean  
 415 daily precipitation differences (shading, mm) and CAPE (contours, J kg<sup>-1</sup>) on 29 October. For CAPE, only positive differences  
 above 100 J kg<sup>-1</sup> are shown. (c) Hourly differences in precipitation rate (orange) and accumulated precipitation (black) over VAL.  
 Solid lines indicate the mean difference, and shading shows the minimum–maximum range. Accumulated precipitation is  
 computed starting at 00 UTC on 24 October. (d) As in (c), but for CAPE (orange) and vertically-averaged vertical velocity (black).  
 (e) As in (d), but for hourly differences in IVTx over VAL (orange), NWA (blue), and MED (green). (f) As in (e), but for IVTy. (g)  
 As in (f), but for TCWV. The shading in panels (c) to (g) shows the minimum-maximum range obtained using all the ensemble  
 members.

420 On 29 October, the Factual–Counterfactual differences in equivalent potential temperature ( $\theta_e$ ) are maximised in the lower  
 troposphere, with the strongest anomalies below 600–700 hPa (Fig. 5b). These enhanced low-level  $\theta_e$  differences coincide  
 with the period of strongest mid-tropospheric ascent and with a marked increase in near-surface dew point temperature (Fig.  
 7 in the Supplement), suggesting a strengthened coupling between low-level moist instability and upward motion during the  
 peak of the event.

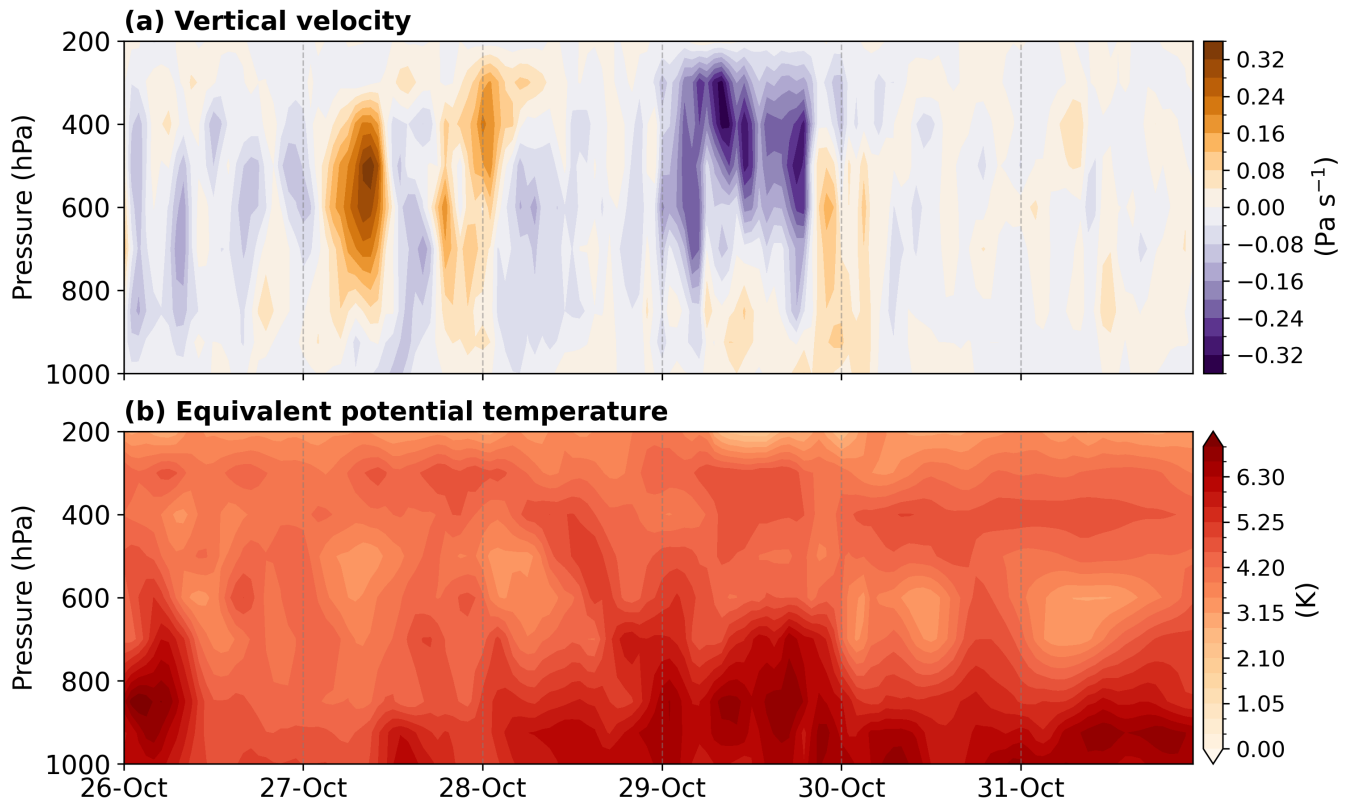


**Figure 5: Time-pressure evolution of Factual – Counterfactual differences in (a) vertical velocity ( $\Omega$ , in Pa/s) and (b) equivalent potential temperature ( $\theta_e$ , in K) over the VAL region.**

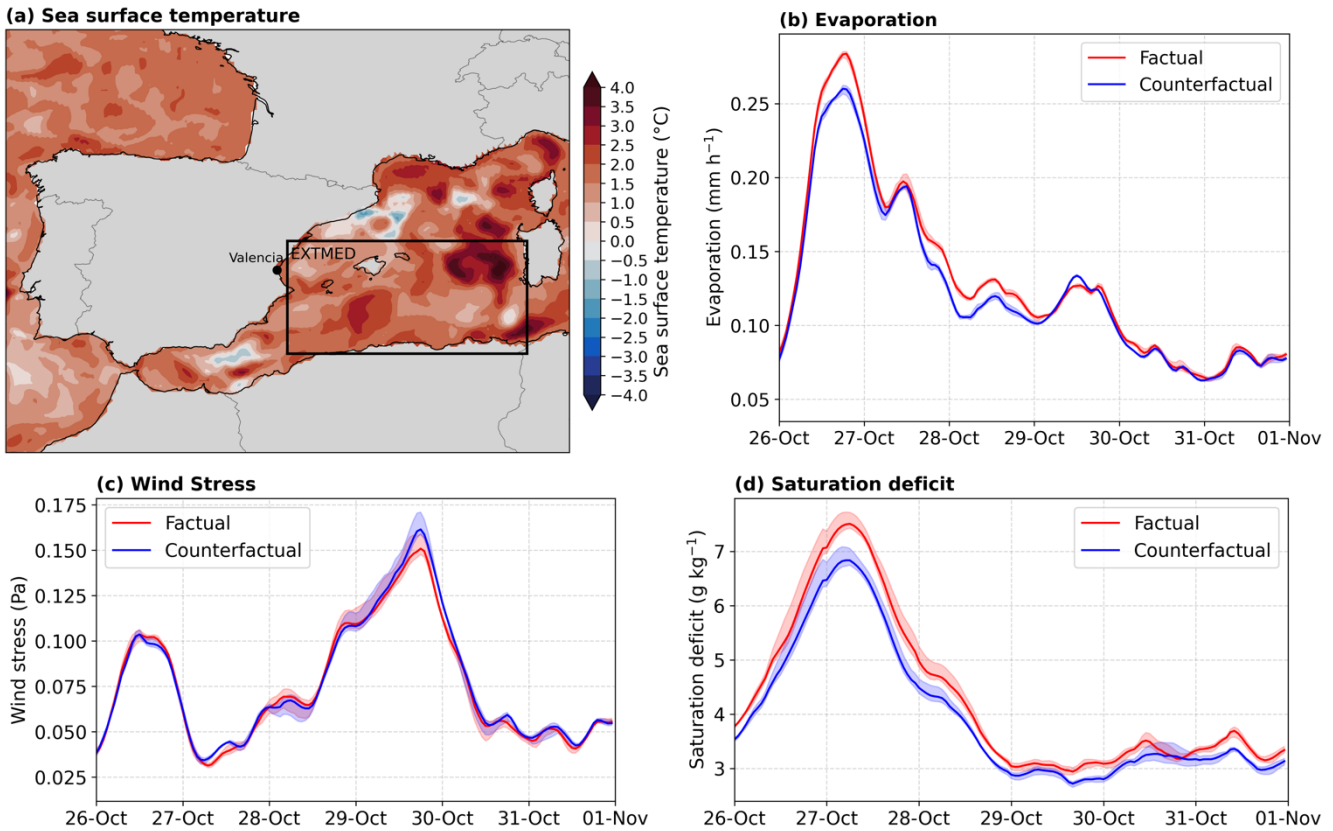
430 **Table 1** summarises the relative changes between the Factual and Counterfactual scenarios (Eq. 2) over the main regions and variables discussed above. Overall, the results indicate a coherent thermodynamic response to global warming, with consistent increases across all variables. The largest relative change is observed in precipitation rate over VAL, with a mean increase of 36% and a range of 14% to 57% across ensemble members. Accumulated precipitation over the 24-29 October period also increases by 20% on average. CAPE exhibits a substantial rise of about 25%, indicating enhanced atmospheric

435 instability under warmer conditions. The moisture-related variables (TCWV and IVT) show more moderate but spatially consistent increases of 15-25% across the three regions, with the strongest relative changes in TCWV and IVT over NWA, reflecting the intensified subtropical moisture inflow that feeds the AR-like structure.

440 **Table 1: Relative changes between the Factual and Counterfactual scenarios. \*For precipitation rate and CAPE, only 29 October is considered. +Accumulated precipitation corresponds to the period from 24-29 October. The maximum–minimum range is estimated across all ensemble members.**

Variable	Min (%)	Mean (%)	Max (%)
Precipitation rate (VAL)*	14	36	57
Accumulated precipitation (VAL)	15	20	26
CAPE (VAL)*	6	25	42
IVT (VAL)	13	19	24
IVT (MED)	15	18	22
IVT (NWA)	23	25	28
TCWV (VAL)	15	18	21
TCWV (MED)	18	20	21
TCWV (NWA)	22	24	26

The SST over the Mediterranean Sea is higher in the Factual scenario, with an average increase of nearly 2°C and localised areas exceeding 3°C of increase (Fig. 6a). In the EXTMED region, the mean SST in the Factual scenario is about 22.5-23°C, compared to ~21°C in the Counterfactual scenario (Fig. 3d). These warmer SSTs are associated with enhanced evaporation, contributing to a moister environment near the coast of Valencia. In the days preceding 29 October, evaporation shows a maximum in both scenarios, associated with the advection of cold and dry air over the EXTMED linked to the COL. During this period, evaporation is notably higher in the Factual scenario than in the Counterfactual; primarily driven by differences in the thermodynamic component, while differences in wind stress are negligible (Fig. 6). On 29 October, surface winds contribute to relative increases in evaporation, but the differences in evaporation between scenarios remain negligible (Fig. 6). The limited dynamical differences between scenarios may partly reflect the spectrally nudged configuration of the simulations, which constrains the large-scale circulation above 700 hPa and thereby emphasises thermodynamic contrasts between climate states. The overall relative change in evaporation is 5.5% (range: 4.5-6%). These findings suggest that climate change may have played a significant role in increasing moisture availability and thereby creating favourable conditions for the intense precipitation observed during the event.



460 **Figure 6: (a) Mean SST difference between the Factual and Counterfactual scenarios, averaged over 24-31 October. Hourly evolution of (a) evaporation ( $\text{mm h}^{-1}$ ), (b) wind stress (Pa), and (c) saturation deficit ( $\text{g kg}^{-1}$ ) over the extended Mediterranean (EXTMED; box in panel a) for the Factual (red) and Counterfactual (blue) scenarios. Shading shows all the ensemble members.**

### 3.4 Signal-to-noise ratio analysis

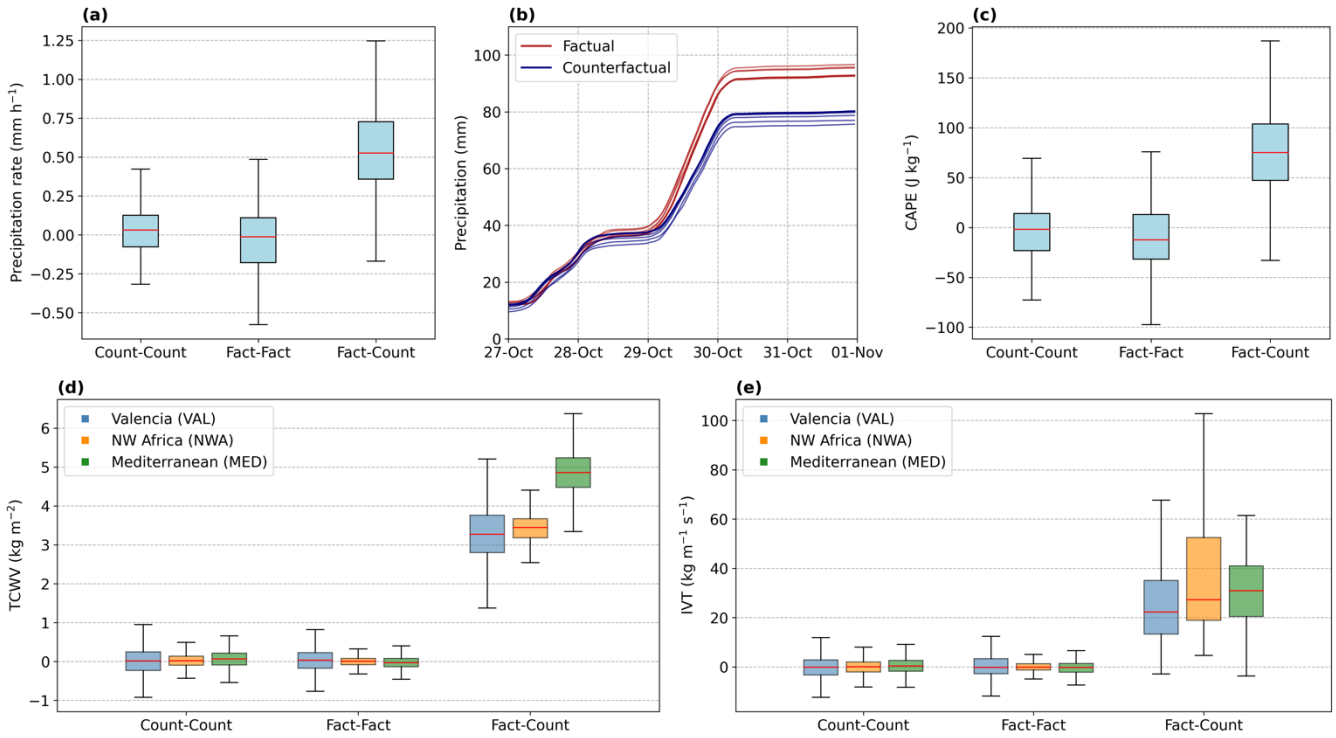
To strengthen the robustness of the findings presented in the previous section, we apply a signal-to-noise ratio approach to disentangle the climate change signal from internal variability. Specifically, we test whether the differences between ensemble members of the Factual and Counterfactual scenarios are statistically distinguishable from the variability observed within each scenario.

465

In general, the climate change signal is detectable across all variables. The intra-scenario distributions (for the Counterfactual, Count–Count, and the Factual, Fact–Fact) show median values and interquartile ranges centred around zero, whereas the inter-scenario distributions (Fact–Count) exhibit positive median values and interquartile ranges (Fig. 7). For the moisture-related variables, TCWV and IVT, the climate change signal clearly emerges from the noise, as the median and the 25th percentile of the inter-scenario distribution exceed the 75th percentile of the intra-scenario distributions in all regions

470

(Fig. 7d-e). This separation is particularly pronounced for TCWV, where even the 5th percentile of the inter-scenario distribution lies above the 95th percentile of the intra-scenario distributions. Similar results are observed for SST, while for evaporation, the signal is less pronounced (Fig. S8 in the Supplement).



480 **Figure 7: Distribution of hourly differences between ensemble members for the Counterfactual scenario (Count-Count), the Factual scenario (Fact-Fact), and between scenarios (Fact-Count) for (a) precipitation rate over VAL on 29 October, (c) as in (a) but for CAPE, (d) TCWV over VAL (blue), NWA (orange), and MED (green) for the 24-31 October period, and (e) as in (d) but for IVT. (b) Accumulated precipitation over VAL for ensemble members of the Factual (red) and Counterfactual (blue) scenarios. Bold lines indicate the main run. Accumulation is calculated from 24 October. The boxes show the interquartile range of the distribution (25th-75th percentiles), the red line the median (50th percentile), and the vertical bars the 5th-95th percentile range. Outliers have been removed.**

485

For the precipitation rate, a significant climate change signal is detected on 29 October (Fig. 7a). In contrast, no clear separation between scenarios is observed for the rainfall of the preceding days. The accumulated precipitation from 24 to 28 October is indistinguishable across ensemble members of both scenarios, with totals around 40 mm. On 29 October, however, the ensemble curves start to diverge markedly, leading to a clear difference in total accumulated rainfall by the end of the period (Fig. 7b). The analysis for CAPE is similarly restricted to 29 October, as this is when the most distinct signal emerges (Fig. 7c).

490

These results suggest that the influence of climate change on precipitation becomes evident only beyond a certain intensity threshold. Moderate and light rainfall events remain within the range of internal variability, while heavier precipitation shows a clear positive response to the additional warming. A similar behaviour is observed outside the VAL region, particularly over southern Spain, where the exceedance probabilities between scenarios start to diverge for rates exceeding  $\sim 5 \text{ mm h}^{-1}$  (Fig. S9 in the Supplement).

#### 4 Discussion and conclusions

Recent attribution studies of the October 2024 Valencia extreme precipitation event (EPE) have reported differing estimates of the influence of anthropogenic climate change depending on the methodological framework employed. Probabilistic and circulation-conditioned approaches have yielded mixed results regarding changes in event probability and precipitation intensity, ranging from substantial increases under present-day warming conditions (WWA, 2024) to weak or statistically non-significant changes (Barriopedro et al., 2025; Oldham-Dorrington & Messori, 2026). Studies using regional-to-local storylines under the pseudo-global warming approach consistently identify a robust thermodynamic amplification of the event under present-day climate conditions (Barriopedro et al., 2025; Calvo-Sancho et al., 2026). These contrasting results highlight the difficulty of attributing highly complex precipitation extremes using probabilistic approaches alone, motivating complementary frameworks that explicitly examine the physical processes through which anthropogenic warming influences the event (Van Garderen & León-FonFay, 2026).

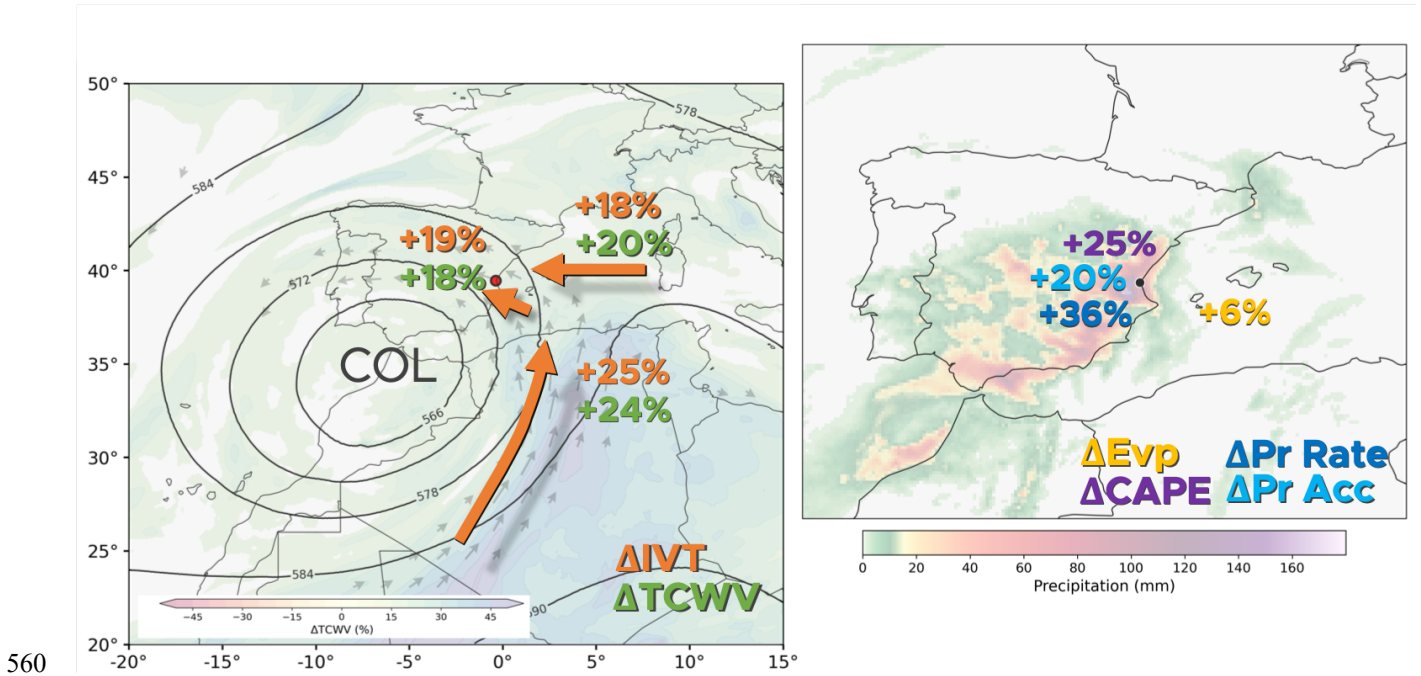
Building on previous attribution studies, we analyse the spatiotemporal evolution of the synoptic-scale thermodynamic drivers of the event using kilometre-scale spectrally nudged global simulations from the DestinE ClimateDT initiative (Doblas-Reyes et al., 2026), in which the observed large-scale evolution of the Valencia EPE is preserved across Factual (present-day) and Counterfactual ( $\sim 1950$ s) climate scenarios within a coupled modelling framework (John et al., 2026). Our analysis particularly addresses the moisture transport and atmosphere-ocean preconditioning associated with the cut-off low (COL) over the WMed in late October 2024. The present study shows that anthropogenic climate change significantly contributed to enhanced atmospheric moisture availability, moisture transport, and instability, leading to a significant increase in the precipitation over Valencia. At the same time, we show that both precipitation and its thermodynamic drivers were also extreme under Counterfactual conditions during the event. Together, these results suggest that the Valencia EPE emerged from the combination of a favourable synoptic configuration and a substantial thermodynamic amplification associated with anthropogenic warming.

In particular, we estimate that the atmospheric moisture content and transport increased by approximately 20% under present-climate conditions (Fig. 8), which is physically consistent with the Clausius-Clapeyron (CC) relationship (Held & Soden, 2006), given the  $\sim 2.2^\circ\text{C}$  surface temperature difference between scenarios in our simulations (based on the 8-year

525 mean 2 metres air temperature over the 30°-60°N, 50°W-10°E domain; not shown). Previous estimates also point to a  
climate-change-induced moistening of the event, although the magnitude of the response differs depending on the variable,  
spatio-temporal scale, and counterfactual definition considered. [Barriopedro et al. \(2025\)](#) reported an approximately 5%  
increase in specific humidity at 850 hPa, together with an intensification of warm and moist low-level air advection from the  
Mediterranean Sea toward the Valencia region during the peak of the event. At a more local scale, [Calvo-Sancho et al.](#)  
530 [\(2026\)](#) reported increases of about 12% in precipitable water and 8.5% in water vapour flux into the storm over Valencia.  
Together, these findings support the interpretation that climate change amplified the thermodynamic environment of the  
Valencia EPE, consistent with previous studies highlighting the role of warming-induced moisture increases in enhancing the  
potential for extreme precipitation ([O’Gorman & Muller, 2010](#); [Schneider et al., 2010](#)).

535 Beyond this broad moistening signal, our results show that the thermodynamic amplification was not spatially homogeneous,  
but was more pronounced along the atmospheric river-like (AR-like) moisture plume extending from northwestern Africa  
toward the Iberian Peninsula. In this structure, atmospheric moisture content and transport increased by up to ~25% under  
present-climate conditions ([Fig. 8](#)). This synoptic-scale perspective complements previous regional and storm-scale studies  
by showing where the additional moisture was organised and transported before reaching the Valencia region. In addition,  
540 we show that Mediterranean Sea surface temperatures were significantly warmer under present-climate conditions, favouring  
enhanced evaporation and low-level moisture availability prior to the peak of the event. Similarly, [Calvo-Sancho et al.](#)  
[\(2026\)](#) previously reported an increase in evaporation near the Valencian coast. However, our results extend this local  
perspective by showing that enhanced evaporation was not limited to the immediate coastal area, but was also evident over a  
broader Mediterranean region during the days preceding the precipitation peak. This provides a physical link between  
545 anthropogenic warming and the warm Mediterranean conditions previously identified as an important contributor to the  
event ([Saurral et al., 2026](#)).

The thermodynamic amplification of the synoptic environment translated into a substantial and highly nonlinear increase in  
precipitation intensity over the Valencia region. Under 1950s climate conditions, the same synoptic configuration produced  
550 approximately 20% less precipitation over Valencia than under present-day conditions ([Fig. 8](#)). This apparently modest  
change translates into a non-linear response in the spatial extent of extreme rainfall. For instance, the area exceeding the 90th  
percentile of daily precipitation doubled under present-day conditions, while the area exceeding the 99th percentile increased  
nearly fivefold (not shown). These estimates are in close agreement with previous attribution studies. In particular,  
[Barriopedro et al. \(2025\)](#) reported an approximately 20% increase in accumulated precipitation, while [Calvo-Sancho et al.](#)  
555 [\(2026\)](#) found a comparable expansion of the area affected by extreme rainfall. The convergence of these results across  
distinct process-based attribution approaches strengthens the evidence for a robust thermodynamic contribution of  
anthropogenic warming to the precipitation response of the Valencia EPE.



560

**Figure 8: Schematic figure of the relative changes between Factual and Counterfactual scenarios. Total column water vapor ( $\Delta TCWV$ , in green) and integrated water vapour transport ( $\Delta IVT$ , in orange) on the left. Precipitation rate ( $\Delta Pr$  Rate, in dark blue), accumulated precipitation ( $\Delta Pr$  Acc, in light blue), evaporation ( $\Delta Evp$ , in yellow) and most unstable convective available potential energy ( $\Delta CAPE$ , in purple) on the right.**

565

The strongest precipitation amplification occurred on the peak of the event, on 29 October, when precipitation rates in the Factual scenario were approximately 36% higher than under 1950s climate conditions (Fig. 8). This increase substantially exceeds the thermodynamic scaling expected from the mean warming signal alone and is consistent with previous studies showing that short-duration and convective precipitation extremes can intensify beyond CC scaling (Formayer & Fritz, 2017; Fowler et al., 2021; Guerreiro et al., 2018). Several processes likely contributed to this super-CC behaviour, including enhanced moisture transport and convergence on 29 October partly driven by the AR-like structure, consistent with previous studies highlighting the key role of large-scale moisture fluxes in modulating precipitation intensity (Gimeno-Sotelo & Gimeno, 2023; Prein et al., 2017). Additionally, the largest inter-scenario differences in mid-tropospheric vertical velocity and low-level equivalent potential temperature occurred on 29 October, when near-surface dew point temperatures also increased substantially. These results suggest that, beyond the increased moisture availability, a non-linear dynamical response contributed to the extreme precipitation, with latent heat release likely intensifying the updrafts as previously documented for this and other convective events (Calvo-Sancho et al., 2026; Fowler et al., 2021; Lenderink et al., 2017; Molnar et al., 2015; Singleton & Toumi, 2013).

575

580 The simulations used in this study, developed within the DestinE ClimateDT initiative (Doblas-Reyes et al., 2026), provide a novel opportunity for systematic event-based storyline attribution at the global scale. Their continuous, coupled, kilometre-scale configuration enables the thermodynamic influence of climate change to be assessed for extreme events occurring worldwide from 2018 onward within a common modelling framework (John et al., 2026). Compared with limited-area regional experiments, the global domain allows the large-scale circulation to be analysed consistently across climate  
585 scenarios, while still retaining kilometre-scale resolution to link synoptic-scale drivers to local precipitation responses, as illustrated here for the Valencia EPE. This represents an important step for the attribution community, as it allows physically consistent comparisons between factual and counterfactual climate states beyond region-specific or event-specific experimental setups.

590 Several limitations should be acknowledged. First, the use of spectral nudging constrains the large-scale atmospheric circulation, limiting the ability of the simulated dynamics to fully adjust to thermodynamic changes in temperature and moisture; the implications of this limitation for the attribution of extreme events should be further investigated to quantify potential under- or overestimations. This design is well suited to isolating thermodynamic effects under a prescribed synoptic evolution, but it also means that potential climate-change influences on the dynamics of the event itself, such as changes in  
595 the trajectory or location of the circulation pattern, are not directly assessed. Second, the Counterfactual scenario represents a cooler 1950-like climate state rather than a fully pre-industrial world (John et al., 2026). This choice, which follows the experimental design of the DestinE ClimateDT storyline simulations, introduces additional uncertainty when interpreting the results as an anthropogenic climate-change signal, although it may also be useful for impact-oriented storylines in cases where the mid-twentieth century provides a meaningful reference period for exposure and vulnerability. Finally, the 9-km  
600 horizontal resolution remains insufficient to fully resolve local-scale precipitation extremes in complex coastal and mountainous regions such as Valencia, where even convection-permitting regional climate models often struggle to reproduce the observed intensity and spatial variability (Calvo-Sancho et al., 2026).

Future work could extend this analysis in several directions. A key open question concerns the possible influence of  
605 anthropogenic climate change on the dynamical component of the event, including whether the frequency, persistence, or preferred location of quasi-stationary COLs over the western Mediterranean has changed or may change in the future. Future studies could also move beyond meteorological attribution toward impact attribution (Noy et al., 2024), using hydrological and flood-modelling approaches to translate changes in precipitation intensity, spatial extent, and timing into changes in runoff, and flood severity (e.g., Versteeg et al., 2026). Coupling climate attribution with exposure and vulnerability analyses  
610 would be particularly important for assessing how climate change, land-use change, urban development, and flood-management infrastructure jointly shaped the observed impacts. In this sense, the present study should be viewed as one line of evidence within a broader multi-method attribution framework.

## Appendix A: Acronyms

<b>AEMET</b>	Spanish Meteorological Agency (Agencia Estatal de Meteorología)
<b>AR</b>	Atmospheric river
<b>ASL</b>	Above sea level
<b>AVAMET</b>	Valencian Meteorological Association (Associació Valenciana de Meteorologia)
<b>CAPE</b>	Convective available potential energy
<b>CC</b>	Clausius-Clapeyron
<b>ClimateDT</b>	Digital Twins for climate adaptation
<b>COL</b>	Cut-off low
<b>DANA</b>	Upper-level isolated depression (Depresión Aislada en Niveles Altos)
<b>DestinE</b>	Destination Earth
<b>EERIE</b>	European Eddy RIch Earth System Models
<b>EPE</b>	Extreme precipitation event
<b>ERA5</b>	ECMWF reanalysis version 5
<b>ETCCDI</b>	Expert team on climate change detection and indices
<b>EXTMED</b>	Extended Mediterranean box
<b>FESOM</b>	Finite volumE Sea Ice-Ocean Model
<b>GDAS</b>	Global Data Assimilation System
<b>HYSPLIT</b>	HYbrid Single Particle Lagrangian Integrated Trajectory model
<b>IFS</b>	Integrated Forecasting System
<b>IVT</b>	Integrated water vapour transport
<b>MED</b>	Mediterranean box
<b>MSLP</b>	Mean sea level pressure
<b>MSWEP</b>	Multi-Source Weighted-Ensemble Precipitation
<b>NOAA</b>	National Oceanic and Atmospheric Administration
<b>NWA</b>	Northwestern Africa box
<b>OISST</b>	Optimum Interpolation Sea Surface Temperature

<b>Rx1day</b>	Maximum daily precipitation index
<b>SST</b>	Sea surface temperature
<b>TCWV</b>	Total column water vapour
<b>UTC</b>	Coordinated Universal Time
<b>VAL</b>	Valencia box
<b>WMed</b>	Western Mediterranean

### Code availability

615 All the Jupyter Notebooks and codes used for the analysis will be available in a GitHub repository after acceptance.

### Data availability

Data from the IFS-FESOM storyline runs are available through the DestinE DESP platform <https://destine-data-lake-docs.data.destination-earth.eu/en/latest/introduction/introduction.html>. Data from the long IFS-FESOM run is available through the World Data Center for Climate platform [https://www.wdc-climate.de/ui/entry?acronym=EERIE\\_FESOM\\_hist\\_v1](https://www.wdc-climate.de/ui/entry?acronym=EERIE_FESOM_hist_v1). ERA5 reanalysis and E-OBS data are accessible via the Copernicus Climate Data Store <https://cds.climate.copernicus.eu/datasets>. MSWEP data is accessible via the NCAR Climate Data Guide <https://climatedataguide.ucar.edu/climate-data/global-high-resolution-precipitation-mswep>. NOAA OISSTv2 dataset is available on the NOAA Physical Sciences Laboratory webpage <https://psl.noaa.gov/data/gridded/data.noaa.oisst.v2.highres.html>. Daily precipitation data from AEMET is available here <https://opendata.aemet.es/centrodedescargas/productosAEMET>. Daily precipitation data from AVAMET are available here <https://www.avamet.org/mx-meteoxarxa.php>. The HYSPLIT model can be run at the NOAA Air Resources Laboratory portal <https://www.ready.noaa.gov/HYSPLIT.php>.

### Author contribution

DC, KG and RS designed the methodology for the study. SB and AJ prepared and ran the storyline simulations. DC  
 630 conducted the analyses, produced the visualisations, and wrote the paper. MO and FDR supervised. All the authors contributed to the review and editing process.

### **Competing interests**

The authors declare that they have no conflict of interest.

### **Acknowledgements**

635 We would like to acknowledge the European Commission Destination Earth Program and the GLORIA project funded by the Spanish MICIU/AEI and by the European Union NextGenerationEU/PRTR. We also acknowledge the EERIE project.

### **Financial support**

RIS and MO are funded by the AI4Science PN070500 fellowship within the “Generación D” initiative, Red.es, Ministerio para la Transformación Digital y de la Funi3n P3blica, for talent attraction (C005/24-ED CV1). Funded by the European  
640 Union NextGenerationEU funds, through PRTR.

## References

- AEMET. (2024). Estudio sobre la situación de lluvias intensas, localmente torrenciales y persistentes, en la Península Ibérica y Baleares entre los días 28 de octubre y 4 de noviembre de 2024. Agencia Estatal de Meteorología.
- 645 Alpert, P., Ben-Gai, T., Baharad, A., Benjamini, Y., Yekutieli, D., Colacino, M., Diodato, L., Ramis, C., Homar, V., Romero, R., Michaelides, S., & Manes, A. (2002). The paradoxical increase of Mediterranean extreme daily rainfall in spite of decrease in total values. *Geophysical Research Letters*, 29(11). <https://doi.org/10.1029/2001GL013554>
- Barrett, B. S., Campos, D. A., Veloso, J. V., & Rondanelli, R. (2016). Extreme temperature and precipitation events in March 2015 in central and northern Chile. *Journal of Geophysical Research: Atmospheres*, 121(9), 4563–4580. <https://doi.org/10.1002/2016JD024835>
- 650 Barriopedro, D., Jiménez-Esteve, B., Collazo, S., Garrido-Perez, J. M., Johnson, J. E., & García-Herrera, R. (2025). A multi-method attribution analysis of the Spain's 2024 extreme precipitation event. *Bulletin of the American Meteorological Society*, BAMS-D-25-0049.1. <https://doi.org/10.1175/BAMS-D-25-0049.1>
- 655 Beck, H. E., Wood, E. F., Pan, M., Fisher, C. K., Miralles, D. G., Van Dijk, A. I. J. M., McVicar, T. R., & Adler, R. F. (2019). MSWEP V2 Global 3-Hourly 0.1° Precipitation: Methodology and Quantitative Assessment. *Bulletin of the American Meteorological Society*, 100(3), 473–500. <https://doi.org/10.1175/BAMS-D-17-0138.1>
- Bozkurt, D., Rondanelli, R., Garreaud, R., & Arriagada, A. (2016). Impact of warmer eastern tropical Pacific SST on the March 2015 Atacama floods. *Monthly Weather Review*, 144(11), 4441–4460.
- 660 Brenowitz, N. D., Cohen, Y., Pathak, J., Mahesh, A., Bonev, B., Kurth, T., Durran, D. R., Harrington, P., & Pritchard, M. S. (2025). A Practical Probabilistic Benchmark for AI Weather Models. *Geophysical Research Letters*, 52(7), e2024GL113656. <https://doi.org/10.1029/2024GL113656>
- Calvo-Sancho, C., Díaz-Fernández, J., González-Alemán, J. J., Halifa-Marín, A., Miglietta, M. M., Azorin-Molina, C., Prein, A. F., Montoro-Mendoza, A., Bolgiani, P., Morata, A., & Martín, M. L. (2026). Human-induced climate change amplification on storm dynamics in Valencia's 2024 catastrophic flash flood. *Nature Communications*, 17(1), 1492. <https://doi.org/10.1038/s41467-026-68929-9>
- 665 Campos, D. A., Olmo, M. E., Cos, P., Muñoz, Á. G., & Doblas-Reyes, F. J. (2025). Regional Aspects of Observed Temperature and Precipitation Trends in the Western Mediterranean: Insights From a Timescale Decomposition Analysis. *Journal of Geophysical Research: Atmospheres*, 130(19), e2024JD042637. <https://doi.org/10.1029/2024JD042637>
- 670 Chericoni, M., Fosser, G., Flaounas, E., Gaetani, M., & Anav, A. (2025). Unravelling drivers of the future Mediterranean precipitation paradox during cyclones. *Npj Climate and Atmospheric Science*, 8(1), 260. <https://doi.org/10.1038/s41612-025-01121-w>

- Copernicus Climate Change Service. (2018). ERA5 hourly data on pressure levels from 1940 to present [Dataset]. Copernicus Climate Change Service (C3S) Climate Data Store (CDS). <https://doi.org/10.24381/CDS.BD0915C6>
- 675 Cornes, R. C., Van Der Schrier, G., Van Den Besselaar, E. J. M., & Jones, P. D. (2018). An Ensemble Version of the E-OBS Temperature and Precipitation Data Sets. *Journal of Geophysical Research: Atmospheres*, 123(17), 9391–9409. <https://doi.org/10.1029/2017JD028200>
- Cos, J., Doblas-Reyes, F., Jury, M., Marcos, R., Bretonnière, P.-A., & Samsó, M. (2022). The Mediterranean climate change hotspot in the CMIP5 and CMIP6 projections. *Earth Syst. Dynam.*, 13(1), 321–340. <https://doi.org/10.5194/esd-13-321-2022>
- Danilov, S., Sidorenko, D., Wang, Q., & Jung, T. (2017). The Finite-volumE Sea ice–Ocean Model (FESOM2). *Geoscientific Model Development*, 10(2), 765–789. <https://doi.org/10.5194/gmd-10-765-2017>
- 680 Doblas-Reyes, F. J., Kontkanen, J., Sandu, I., Acosta, M., Al Turjman, M. H., Alsina-Ferrer, I., Andrés-Martínez, M., Anerdi, C., Arriola, L., Axness, M., Batlle Martín, M., Bauer, P., Becker, T., Beltrán, D., Beyer, S., Bockelmann, H., Bretonnière, P.-A., Cabaniols, S., Caprioli, S., ... Zimmermann, J. (2026). The Destination Earth digital twin for climate change adaptation. *Geoscientific Model Development*, 19(7), 2821–2848. <https://doi.org/10.5194/gmd-19-2821-2026>
- 685 Drobinski, P., Silva, N. D., Panthou, G., Bastin, S., Muller, C., Ahrens, B., Borga, M., Conte, D., Fossier, G., Giorgi, F., Güttler, I., Kotroni, V., Li, L., Morin, E., Önal, B., Quintana-Segui, P., Romera, R., & Torma, C. Z. (2018). Scaling precipitation extremes with temperature in the Mediterranean: Past climate assessment and projection in anthropogenic scenarios. *Climate Dynamics*, 51(3), 1237–1257. <https://doi.org/10.1007/s00382-016-3083-x>
- ECMWF. (2023). ECMWF Newsletter 176: IFS upgrade brings many improvements and unifies medium-range resolutions. <https://www.ecmwf.int/en/newsletter/176/earth-system-science/ifs-upgrade-brings-many-improvements-and-unifies-medium>
- 690 Faranda, D., Alvarez-Castro, M. C., Ginesta, M., Coppola, E., & Pons, F. M. E. (2024). Heavy precipitations in October 2024 South-Eastern Spain DANA mostly strengthened by human-driven climate change. *ClimaMeter*, Institut Pierre Simon Laplace, CNRS. <https://doi.org/10.5281/ZENODO.14052041>
- Feser, F., & Shepherd, T. G. (2025). The concept of spectrally nudged storylines for extreme event attribution. *Communications Earth & Environment*, 6(1), 677. <https://doi.org/10.1038/s43247-025-02659-6>
- 695 Formayer, H., & Fritz, A. (2017). Temperature dependency of hourly precipitation intensities - surface versus cloud layer temperature: PRECIPITATION INTENSITIES: SURFACE VERSUS CLOUD LAYER TEMPERATURE. *International Journal of Climatology*, 37(1), 1–10. <https://doi.org/10.1002/joc.4678>
- Fowler, H. J., Lenderink, G., Prein, A. F., Westra, S., Allan, R. P., Ban, N., Barbero, R., Berg, P., Blenkinsop, S., Do, H. X., Guerreiro, S., Haerter, J. O., Kendon, E. J., Lewis, E., Schaer, C., Sharma, A., Villarini, G., Wasko, C., & Zhang, X. (2021).

- 700 Anthropogenic intensification of short-duration rainfall extremes. *Nature Reviews Earth & Environment*, 2(2), 107–122. <https://doi.org/10.1038/s43017-020-00128-6>
- Ghosh, R., Cheedela, S. K., Wickramage, C., Wachsmann, F., Beyer, S., Aengenheyster, M., Becker, T., Rackow, T., Koldunov, N., Sidorenko, D., & Jung, T. (2025). EERIE: Ocean Eddy-rich Kilometer-scale Climate Simulation with Integrated Forecasting System (IFS) - Finite volumE Sea Ice-Ocean Model (FESOM2.5): historical simulation (Version 1) (Version 1, p. 27110209466186 Bytes) [Application/x-netcdf]. World Data Center for Climate (WDCC) at DKRZ. [https://doi.org/10.26050/WDCC/EERIE\\_FESOM\\_HIST\\_V1](https://doi.org/10.26050/WDCC/EERIE_FESOM_HIST_V1)
- 705
- Jimeno-Sotelo, L., & Jimeno, L. (2023). Where does the link between atmospheric moisture transport and extreme precipitation matter? *Weather and Climate Extremes*, 39, 100536. <https://doi.org/10.1016/j.wace.2022.100536>
- Giorgi, F. (2006). Climate change hot-spots. *Geophysical Research Letters*, 33(8), 2006GL025734. <https://doi.org/10.1029/2006GL025734>
- 710
- Grayson, K., Campos, D., Beyer, S., John, A., Versteeg, G., Kelbling, M., Chandrasekar, A., Thober, S., & Doblus-Reyes, F. J. (2026). Reconstructing storm Gloria in a changing climate using physical storylines. *Npj Natural Hazards*, 3(1), 14. <https://doi.org/10.1038/s44304-026-00174-y>
- Guerreiro, S. B., Fowler, H. J., Barbero, R., Westra, S., Lenderink, G., Blenkinsop, S., Lewis, E., & Li, X.-F. (2018). Detection of continental-scale intensification of hourly rainfall extremes. *Nature Climate Change*, 8(9), 803–807. <https://doi.org/10.1038/s41558-018-0245-3>
- 715
- Held, I. M., & Soden, B. J. (2006). Robust responses of the hydrological cycle to global warming. *Journal of Climate*, 19(21), 5686–5699.
- Hoffmann, J., Bauer, P., Sandu, I., Wedi, N., Geenen, T., & Thiemert, D. (2023). Destination Earth – A digital twin in support of climate services. *Climate Services*, 30, 100394. <https://doi.org/10.1016/j.cliser.2023.100394>
- 720
- Huang, B., Liu, C., Banzon, V., Freeman, E., Graham, G., Hankins, B., Smith, T., & Zhang, H.-M. (2021). Improvements of the Daily Optimum Interpolation Sea Surface Temperature (DOISST) Version 2.1. *Journal of Climate*, 34(8), 2923–2939. <https://doi.org/10.1175/JCLI-D-20-0166.1>
- Huang, T., Fu, S., Li, X., Dong, Y., Zhang, Y., & Sun, J. (2025). Synoptic background conditions and moisture transport for producing the extreme heavy rainfall event in Valencia in 2024. *Atmospheric and Oceanic Science Letters*, 18(6), 100666. <https://doi.org/10.1016/j.aosl.2025.100666>
- 725
- Insua-Costa, D., Miguez-Macho, G., & Llasat, M. C. (2019). Local and remote moisture sources for extreme precipitation: A study of the two catastrophic 1982 western Mediterranean episodes. *Hydrology and Earth System Sciences*, 23(9), 3885–3900. <https://doi.org/10.5194/hess-23-3885-2019>

- 730 IPCC. (2023). *Climate Change 2021 – The Physical Science Basis: Working Group I Contribution to the Sixth Assessment Report of the Intergovernmental Panel on Climate Change* (1st ed.). Cambridge University Press. <https://doi.org/10.1017/9781009157896>
- John, A., Beyer, S., Athanase, M., Sánchez-Benítez, A., Goessling, H. F., Hossain, A., Aguridan, R., Andrés-Martínez, M., Gaya-Àvila, A., Cheedela, S. K., Geier, P., Ghosh, R., Hadade, I., Koldunov, N., Milinski, S., Nurisso, M., Pedruzo-Bagazgoitia, X., Rackow, T., Sandu, I., ... Jung, T. (2026). Global Kilometer-Scale Climate Storylines Using Spectral Nudging. *Journal of Advances in Modeling Earth Systems*, 18(5), e2025MS005326. <https://doi.org/10.1029/2025MS005326>
- Lenderink, G., Barbero, R., Loriaux, J. M., & Fowler, H. J. (2017). Super-Clausius–Clapeyron Scaling of Extreme Hourly Convective Precipitation and Its Relation to Large-Scale Atmospheric Conditions. *Journal of Climate*, 30(15), 6037–6052. <https://doi.org/10.1175/JCLI-D-16-0808.1>
- 740 Lionello, P., & Scarascia, L. (2020). The relation of climate extremes with global warming in the Mediterranean region and its north versus south contrast. *Regional Environmental Change*, 20(1), 31. <https://doi.org/10.1007/s10113-020-01610-z>
- Llasat, M. C. (2024). Spain’s flash floods reveal a desperate need for improved mitigation efforts. *Nature*, 635(8040), 787–787. <https://doi.org/10.1038/d41586-024-03825-0>
- Martin-Moreno, J. M., Garcia-Lopez, E., Guerrero-Fernandez, M., Alfonso-Sanchez, J. L., & Barach, P. (2025). Devastating “DANA” Floods in Valencia: Insights on Resilience, Challenges, and Strategies Addressing Future Disasters. *Public Health Reviews*, 46, 1608297. <https://doi.org/10.3389/phrs.2025.1608297>
- 745 “DANA” Floods in Valencia: Insights on Resilience, Challenges, and Strategies Addressing Future Disasters. *Public Health Reviews*, 46, 1608297. <https://doi.org/10.3389/phrs.2025.1608297>
- May, R. M., Goebbert, K. H., Thielen, J. E., Leeman, J. R., Camron, M. D., Bruick, Z., Bruning, E. C., Manser, R. P., Arms, S. C., & Marsh, P. T. (2022). MetPy: A Meteorological Python Library for Data Analysis and Visualization. *Bulletin of the American Meteorological Society*, 103(10), E2273–E2284. <https://doi.org/10.1175/BAMS-D-21-0125.1>
- 750 Molnar, P., Fatichi, S., Gaál, L., Szolgay, J., & Burlando, P. (2015). Storm type effects on super Clausius–Clapeyron scaling of intense rainstorm properties with air temperature. *Hydrology and Earth System Sciences*, 19(4), 1753–1766. <https://doi.org/10.5194/hess-19-1753-2015>
- Muñoz, C., & Schultz, D. M. (2021). Cutoff Lows, Moisture Plumes, and Their Influence on Extreme-Precipitation Days in Central Chile. *Journal of Applied Meteorology and Climatology*, 60(4), 437–454. <https://doi.org/10.1175/JAMC-D-20-0135.1>
- 755 Cutoff Lows, Moisture Plumes, and Their Influence on Extreme-Precipitation Days in Central Chile. *Journal of Applied Meteorology and Climatology*, 60(4), 437–454. <https://doi.org/10.1175/JAMC-D-20-0135.1>
- Nieto Ferreira, R. (2021). Cut-Off Lows and Extreme Precipitation in Eastern Spain: Current and Future Climate. *Atmosphere*, 12(7), 835. <https://doi.org/10.3390/atmos12070835>
- Noy, I., Stone, D., & Uher, T. (2024). Extreme events impact attribution: A state of the art. *Cell Reports Sustainability*, 1(5), 100101. <https://doi.org/10.1016/j.crsus.2024.100101>

- 760 O’Gorman, P. A., & Muller, C. J. (2010). How closely do changes in surface and column water vapor follow Clausius–Clapeyron scaling in climate change simulations? *Environmental Research Letters*, 5(2), 025207. <https://doi.org/10.1088/1748-9326/5/2/025207>
- Oldham-Dorrington, J., & Messori, G. (2026). Dynamically-Informed Extreme Event Attribution Using Circulation Imprints. *Geophysical Research Letters*, 53(7), e2025GL116869. <https://doi.org/10.1029/2025GL116869>
- 765 Olmo, M. E., Cos, P., Campos, D., Muñoz, A. G., Altava-Ortiz, V., Barrera-Escoda, A., Jury, M., Loosveldt-Tomas, S., Bretonniere, P. A., Doblas-Reyes, F., & Soret, A. (2025). Filtering CMIP6 models in the Euro-Mediterranean based on a circulation patterns approach. *Weather and Climate Extremes*, 100765. <https://doi.org/10.1016/j.wace.2025.100765>
- 770 Porcù, F., Carrassi, A., Medaglia, C. M., Prodi, F., & Mugnai, A. (2007). A study on cut-off low vertical structure and precipitation in the Mediterranean region. *Meteorology and Atmospheric Physics*, 96(1–2), 121–140. <https://doi.org/10.1007/s00703-006-0224-5>
- Prein, A. F., Rasmussen, R. M., Ikeda, K., Liu, C., Clark, M. P., & Holland, G. J. (2017). The future intensification of hourly precipitation extremes. *Nature Climate Change*, 7(1), 48–52. <https://doi.org/10.1038/nclimate3168>
- 775 Rackow, T., Pedruzo-Bagazgoitia, X., Becker, T., Milinski, S., Sandu, I., Aguridan, R., Bechtold, P., Beyer, S., Bidlot, J., Boussetta, S., Deconinck, W., Diamantakis, M., Dueben, P., Dutra, E., Forbes, R., Ghosh, R., Goessling, H. F., Hadade, I., Hegewald, J., ... Ziemann, F. (2025). Multi-year simulations at kilometre scale with the Integrated Forecasting System coupled to FESOM2.5 and NEMOv3.4. *Geoscientific Model Development*, 18(1), 33–69. <https://doi.org/10.5194/gmd-18-33-2025>
- 780 Ribes, A., Thao, S., Vautard, R., Dubuisson, B., Somot, S., Colin, J., Planton, S., & Soubeyroux, J.-M. (2019). Observed increase in extreme daily rainfall in the French Mediterranean. *Climate Dynamics*, 52(1–2), 1095–1114. <https://doi.org/10.1007/s00382-018-4179-2>
- Sánchez-Benítez, A., Goessling, H., Pithan, F., Semmler, T., & Jung, T. (2022). The July 2019 European Heat Wave in a Warmer Climate: Storyline Scenarios with a Coupled Model Using Spectral Nudging. *Journal of Climate*, 35(8), 2373–2390. <https://doi.org/10.1175/JCLI-D-21-0573.1>
- 785 Santer, B. D., Solomon, S., Pallotta, G., Mears, C., Po-Chedley, S., Fu, Q., Wentz, F., Zou, C.-Z., Painter, J., Cvijanovic, I., & Bonfils, C. (2017). Comparing Tropospheric Warming in Climate Models and Satellite Data. *Journal of Climate*, 30(1), 373–392. <https://doi.org/10.1175/JCLI-D-16-0333.1>
- 790 Saurral, R. I., Campos, D. A., Grayson, K., Lapin, V., Trascasa-Castro, P., Tourigny, E., Donat, M. G., Materia, S., Ferrer, E., & Doblas-Reyes, F. J. (2026). The key role of Mediterranean and North Atlantic sea surface temperatures on the 2024 record-breaking Valencia precipitation event. *Weather and Climate Extremes*, 52, 100877. <https://doi.org/10.1016/j.wace.2026.100877>

- Saurral, R. I., Doblas-Reyes, F. J., Screen, J. A., Catto, J. L., Hay, S., & Yu, H. (2025). Western Mediterranean Droughts Fostered by Arctic Sea Ice Loss. *Journal of Climate*, 38(13), 3005–3014. <https://doi.org/10.1175/JCLI-D-25-0066.1>
- Schneider, T., O’Gorman, P. A., & Levine, X. J. (2010). WATER VAPOR AND THE DYNAMICS OF CLIMATE CHANGES. *Reviews of Geophysics*, 48(3), RG3001. <https://doi.org/10.1029/2009RG000302>
- 795 Scholz, P., Sidorenko, D., Gurses, O., Danilov, S., Koldunov, N., Wang, Q., Sein, D., Smolentseva, M., Rakowsky, N., & Jung, T. (2019). Assessment of the Finite-volumE Sea ice-Ocean Model (FESOM2.0) – Part 1: Description of selected key model elements and comparison to its predecessor version. *Geoscientific Model Development*, 12(11), 4875–4899. <https://doi.org/10.5194/gmd-12-4875-2019>
- 800 Shepherd, T. G., Boyd, E., Calel, R. A., Chapman, S. C., Dessai, S., Dima-West, I. M., Fowler, H. J., James, R., Maraun, D., Martius, O., Senior, C. A., Sobel, A. H., Stainforth, D. A., Tett, S. F. B., Trenberth, K. E., Van Den Hurk, B. J. J. M., Watkins, N. W., Wilby, R. L., & Zenghelis, D. A. (2018). Storylines: An alternative approach to representing uncertainty in physical aspects of climate change. *Climatic Change*, 151(3–4), 555–571. <https://doi.org/10.1007/s10584-018-2317-9>
- Singleton, A., & Toumi, R. (2013). Super-Clausius–Clapeyron scaling of rainfall in a model squall line. *Quarterly Journal of the Royal Meteorological Society*, 139(671), 334–339. <https://doi.org/10.1002/qj.1919>
- 805 Stein, A. F., Draxler, R. R., Rolph, G. D., Stunder, B. J. B., Cohen, M. D., & Ngan, F. (2015). NOAA’s HYSPLIT Atmospheric Transport and Dispersion Modeling System. *Bulletin of the American Meteorological Society*, 96(12), 2059–2077. <https://doi.org/10.1175/BAMS-D-14-00110.1>
- Thompson, V., Ermis, S., & Athanase, M. (2025). The need for multi-method extreme event attribution. *Weather*, wea.7779. <https://doi.org/10.1002/wea.7779>
- 810 Trambly, Y., & Somot, S. (2018). Future evolution of extreme precipitation in the Mediterranean. *Climatic Change*, 151(2), 289–302. <https://doi.org/10.1007/s10584-018-2300-5>
- Tsuji, H., & Takayabu, Y. N. (2019). Precipitation Enhancement via the Interplay between Atmospheric Rivers and Cutoff Lows. *Monthly Weather Review*, 147(7), 2451–2466. <https://doi.org/10.1175/MWR-D-18-0358.1>
- Tuel, A., & Eltahir, E. A. B. (2020). Why Is the Mediterranean a Climate Change Hot Spot? *JOURNAL OF CLIMATE*, 33.
- 815 Valenzuela, R., Garreaud, R., Vergara, I., Campos, D., Viale, M., & Rondanelli, R. (2022). An extraordinary dry season precipitation event in the subtropical Andes: Drivers, impacts and predictability. *Weather and Climate Extremes*, 37, 100472. <https://doi.org/10.1016/j.wace.2022.100472>

- 820 Van Garderen, L., Feser, F., & Shepherd, T. G. (2021). A methodology for attributing the role of climate change in extreme events: A global spectrally nudged storyline. *Natural Hazards and Earth System Sciences*, 21(1), 171–186. <https://doi.org/10.5194/nhess-21-171-2021>
- Van Garderen, L., & León-FonFay, D. (2026). The essential role of conditional attribution in understanding complex extreme weather. *Nature Communications*, 17(1), 1539. <https://doi.org/10.1038/s41467-026-69056-1>
- 825 Vertegaal, D. M., Van Den Hurk, B. J. J. M., Couasnon, A., Aleksandrova, N., Bovenschen, T., Gradiyanto, F., Leijnse, T. W. B., Goulart, H. M. D., & Muis, S. (2026). Climate and impact attribution of compound flooding induced by tropical cyclone Idai in Mozambique. *Natural Hazards and Earth System Sciences*, 26(3), 1417–1433. <https://doi.org/10.5194/nhess-26-1417-2026>
- 830 Vicente-Serrano, S. M., Garrido-Perez, J. M., Fernández-Álvarez, J. C., Gimeno-Sotelo, L., Beguería, S., Halifa-Marín, A., Latorre, B., El Kenawy, A. M., Franquesa, M., Adell-Michavila, M., Domínguez-Castro, F., Barriopedro, D., Gimeno-Presa, L., Nieto, R., Azorin-Molina, C., Andres-Martin, M., Gutiérrez, J. M., & García-Herrera, R. (2025). Characteristics of widespread extreme precipitation events in Peninsular Spain and the Balearic Islands: Spatio-temporal dynamics and driving mechanisms. *Climate Dynamics*, 63(9), 340. <https://doi.org/10.1007/s00382-025-07829-y>
- Wedi, N., Bauer, P., Sandu, I., Hoffmann, J., Sheridan, S., Cereceda, R., Quintino, T., Thiemert, D., & Geenen, T. (2022). Destination Earth: High-Performance Computing for Weather and Climate. *Computing in Science & Engineering*, 24(6), 29–37. <https://doi.org/10.1109/MCSE.2023.3260519>
- 835 WWA. (2024, November 4). Extreme downpours increasing in southeastern Spain as fossil fuel emissions heat the climate. <https://www.worldweatherattribution.org/extreme-downpours-increasing-in-southernspain-as-fossil-fuel-emissions-heat-the-climate/>
- 840 Zhang, G. J. (1997). A Further Study on Estimating Surface Evaporation Using Monthly Mean Data: Comparison of Bulk Formulations. *Journal of Climate*, 10(7), 1592–1600. [https://doi.org/10.1175/1520-0442\(1997\)010%3C1592:AFSOES%3E2.0.CO;2](https://doi.org/10.1175/1520-0442(1997)010%3C1592:AFSOES%3E2.0.CO;2)
- Zhang, X., Alexander, L., Hegerl, G. C., Jones, P., Tank, A. K., Peterson, T. C., Trewin, B., & Zwiers, F. W. (2011). Indices for monitoring changes in extremes based on daily temperature and precipitation data. *WIREs Climate Change*, 2(6), 851–870. <https://doi.org/10.1002/wcc.147>
- 845 Zittis, G., Bruggeman, A., & Lelieveld, J. (2021). Revisiting future extreme precipitation trends in the Mediterranean. *Weather and Climate Extremes*, 34, 100380. <https://doi.org/10.1016/j.wace.2021.100380>

